

6

Elements of Phenomenological Plasticity: Geometrical Insight, Computational Algorithms, and Topics in Shock Physics

R.M. Brannon

6.1 Introduction

This chapter reviews the terminology and governing equations of plasticity, with emphasis on amending misconceptions, providing physical insights, and outlining computational algorithms. Plasticity theory is part of a larger class of material models in which a pronounced change in material response occurs when the stress (or strain) reaches a critical threshold level. If the stress state is subcritical, then the material is modeled by classical elasticity. The boundary of the subcritical (elastic) stress states is called the yield surface. Plasticity equations apply if continuing to apply elasticity theory would predict stress states that extend beyond this the yield surface. The onset of plasticity is typically characterized by a pronounced slope change in a stress–strain diagram, but load reversals in experiments are necessary to verify that the slope change is not merely nonlinear elasticity or reversible phase transformation. The threshold yield surface can appear to be significantly affected by the loading rate, which has a dominant effect in shock physics applications.

Following pioneering developments of the early 1900s, modern plasticity theory quickly reached a relatively mature state in the 1950s and 1960s for modeling metals. More recently, aspects of plasticity theory (as a mathematical formalism) have been adopted, rejected, or modified for more complicated materials such as composites and rock-like materials where inelasticity originates from microscale imperfections other than dislocations. Many approximations for metals may not hold for other materials in this broader scope. It is often asserted, e.g., that shock loading pushes stresses well beyond “the” yield stress to make the material flow essentially like a fluid. However, given that no *single* yield stress exists when strength is pressure-dependent, strength actually affects shock waves across a significant range of shock pressures. Likewise, although separation of load–unload curves may be used to infer shear strength for a von Mises material, this separation (in generalized plasticity) is a complicated history-dependent function of pressure-dependent strength,

extension–compression strength differences, hardening, phase transformation, rate dependence, and a host of other simultaneously acting effects.

Generalized plasticity models often assume nonassociativity (nonnormality of the plastic strain rate relative to the yield surface). However, physically undesirable consequences of nonassociativity will be described, along with a list of ways that the direction of the plastic strain rate is often misassessed, possibly giving a false *impression* of nonnormality when the material might be, in fact, associative.

The first half of this chapter outlines the general framework of modern rate-independent plasticity theory, with an emphasis on geometrical interpretations of the equations that guide development of computational algorithms. The second half of this chapter focuses on high-rate applications of plasticity, where the influence of rate sensitivity is illustrated in the context of uniaxial strain loading, which is typical in shock physics applications. The scope of this chapter is limited to plastic *constitutive models*, with essentially no discussion (aside from wave propagation speeds) about the effect of the constitutive model on field-scale simulations.

6.2 Notation and Terminology

Frequently used symbols (stress, strain, etc.) are defined on page 270. Definitions for well-known tensor operations (trace, determinant, etc.) may be found in [5]. Repeated subscripts within indicial expressions are understood to be summed from 1 to 3. Nonrepeated indices are free and take values 1–3. Several equations are written in “direct” notation, where scalars, vectors, second-order tensors, and higher-order tensors are typeset as, e.g., s , \mathbf{v} , \mathbf{T} , and \mathbb{E} , respectively. For incremental equations, a superposed dot denotes a time derivative following the material particle (for rate-independent plasticity, “time” is any monotonically increasing scalar that parameterizes the deformation history). The derivative of a second-order tensor \mathbf{A} with respect to a second-order tensor \mathbf{B} is a fourth-order tensor with $ijkl$ components $\partial A_{ij}/\partial B_{kl}$. In elasticity, the elastic stiffness is the derivative of stress with respect to strain $E_{ijkl} = \partial \sigma_{ij}/\partial \varepsilon_{kl}$. All second-order tensors are presumed symmetric $A_{ij} = A_{ji}$, and all fourth-order tensors are minor-symmetric $E_{ijkl} = E_{jikl} = E_{ijlk}$. Unlike the plastic stiffness tensor, the elastic stiffness tensor is presumed to be always major symmetric ($E_{ijkl} = E_{klij}$).

This chapter follows the mechanics convention that stress and strain are positive in tension. However, because problems in mechanics (especially shock physics) involve compressive stresses and strains, we define an overbar such that, for any variable x ,

$$\bar{x} \equiv -x. \quad (6.1)$$

For example, we define *mean stress* (positive in tension) by

$$p = \frac{1}{3} (\text{tr} \boldsymbol{\sigma}) \equiv \frac{1}{3} \sigma_{kk}. \quad (6.2)$$

Then the *pressure*, which is the negative of mean stress (therefore positive in compression), is denoted \bar{p} .

In materials modeling, tensors are often regarded as higher-dimensional vectors, which can be rigorously justified via the mathematical definition of a vector. The inner product between two tensors ($\mathbf{A} : \mathbf{B} = A_{ij}B_{ij}$) is like the dot product between two vectors ($\mathbf{u} \cdot \mathbf{v} = u_k v_k$). The “magnitude” and “direction” of a tensor are defined analogous to ordinary vector definitions:

$$\text{Magnitude of a vector: } \|\mathbf{v}\| = \sqrt{v_k v_k} = \sqrt{\mathbf{v} \cdot \mathbf{v}}. \quad (6.3)$$

$$\text{Magnitude of a tensor: } \|\mathbf{A}\| = \sqrt{A_{ij}A_{ij}} = \sqrt{\mathbf{A} : \mathbf{A}}. \quad (6.4)$$

$$\text{Direction of a vector } \mathbf{v}: \quad \hat{\mathbf{v}} = \mathbf{v} / \|\mathbf{v}\|. \quad (6.5)$$

$$\text{Direction of a tensor } \mathbf{A}: \quad \hat{\mathbf{A}} = \mathbf{A} / \|\mathbf{A}\|. \quad (6.6)$$

In plasticity theory, the notion of tensor *direction* is used to define the outward normal to the yield surface (which is actually a hypersurface in higher-dimensional tensor space). The angle between two tensors (which is computed analogously to vectors) is essential to quantify the concept of nonnormality, discussed later.

The geometric analogy between the vector dot product and the tensor double-dot extends rigorously to other operations as well. For example, a vector-to-vector linear transformation (denoted $\mathbf{y} = \mathbf{A} \cdot \mathbf{x}$ in direct notation) means $y_i = A_{ik}x_k$. Similarly, a tensor-to-tensor linear transformation (denoted $\mathbf{Y} = \mathbb{E} : \mathbf{X}$) means $Y_{ij} = E_{ijkl}X_{kl}$. In materials modeling, transformations from tensors to tensors (e.g., computing stress from strain) are more prevalent than vector transformations. Just as a second-order tensor may be quantified via a 3×3 component matrix, a minor-symmetric fourth-order tensor is best quantified via a 6×6 *Mandel* (not Voigt [53]) component matrix, the 6-D eigenvectors of which correspond to symmetric *eigentensors*. For example, any deviatoric second-order tensor is an eigentensor of a fourth-order isotropic elastic stiffness, with associated eigenvalue $2G$ where G is the shear modulus. Any isotropic second-order tensor is an eigentensor with eigenvalue $3K$, where K is the bulk modulus.

A vector–vector dyad, \mathbf{uv} , is a second-order tensor with ij components $u_i v_j$. Similarly, a tensor–tensor dyad, \mathbf{AB} , is a fourth-order tensor with $ijkl$ components $A_{ij}B_{kl}$ (not to be confused with tensor composition, which we denote $\mathbf{A} \cdot \mathbf{B}$ with components $A_{ik}B_{kj}$).

In plasticity, the yield threshold is defined by a scalar-valued “yield function” f that depends on the stress (and perhaps a few *internal state variables*, which we will denote η_1, η_2, \dots). Elastic states correspond to $f < 0$, and states at the yield threshold correspond to $f = 0$. Because the equation $f = 0$ defines an isosurface, the normal to the yield surface must be parallel to the gradient of f with respect to stress. For isotropic plasticity, the yield function depends on stress only through its invariants.

Invariants for symmetric tensors always come in independent groups of three. The “mechanics” invariants of a second-order tensor \mathbf{A} are defined

$$J_1^A = \text{tr}\mathbf{A} = A_{kk}, \quad (6.7)$$

$$J_2^A = \frac{1}{2}\text{tr}(\mathbf{A}^d)^2, \quad (6.8)$$

$$J_3^A = \frac{1}{3}\text{tr}(\mathbf{A}^d)^3, \quad (6.9)$$

where “tr” denotes the trace and the superscript “d” denotes the deviatoric part ($\mathbf{A}^d = \mathbf{A} - \frac{1}{3}(\text{tr}\mathbf{A})\mathbf{I}$). Invariants of the stress tensor $\boldsymbol{\sigma}$ are written without a superscript identifier. For example, J_2 means the same thing as J_2^σ . The stress deviator $\mathbf{S} = \boldsymbol{\sigma}^d$ and Hill tensor $\mathbf{T} = (\mathbf{S}^2)^d$, which are defined on page 270, emerge naturally when computing the gradient of any isotropic yield function:

$$\frac{\partial f(I_1, J_2, J_3, \dots)}{\partial \boldsymbol{\sigma}} = \frac{\partial f}{\partial I_1} \mathbf{I} + \frac{\partial f}{\partial J_2} \mathbf{S} + \frac{\partial f}{\partial J_3} \mathbf{T}. \quad (6.10)$$

In isotropic plasticity theory, the three eigenvalues of stress (principal stresses) form an alternative invariant triplet, often regarded as Cartesian coordinates in a 3-D “stress space” (Haigh–Westergaard space). When speaking specifically of *ordered* eigenvalues, we will subscript them with H, M, L (standing for high, middle, and low) so that

$$\sigma_L \leq \sigma_M \leq \sigma_H \quad (6.11)$$

Lode Invariants (r, θ, z) constitute an alternative invariant triplet that is far more useful than mechanics invariants or principal stresses for geometrical visualization of isotropic yield surfaces and for computational implementation. For isotropic plasticity, the yield threshold is characterized by a surface in principal stress space, in which principal stresses are regarded as Cartesian coordinates. Because an isotropic function of principal stresses $f(\sigma_1, \sigma_2, \sigma_3)$ must give the same result regardless of the ordering of the arguments, isotropic yield surfaces have 120° reflective and rotational symmetry about the [111] hydrostat, as in Figs. 6.1 and 6.2.

The Lode invariants merely represent a coordinate change from principal stresses (which are Cartesian coordinates for stress space) to the natural cylindrical coordinates (r, θ, z) for which the z -axis points along the [111] hydrostat (and therefore \bar{z} points along the *compressive* hydrostat). Lode invariants may be computed directly from the mechanics invariants by

$$r = \sqrt{2J_2}, \quad \sin 3\theta = \frac{J_3}{2} \left(\frac{3}{J_2} \right)^{3/2}, \quad z = \frac{I_1}{\sqrt{3}}. \quad (6.12)$$

As illustrated in Fig. 6.2, the Lode angle ranges from -30° in triaxial compression (TXC) to $+30^\circ$ in triaxial extension (TXE). The Lode angle is zero in “shear” states (SHR) where one eigenvalue of the stress deviator is zero and the others are equal but opposite in sign. Triaxial stress states are axisymmetric (two eigenvalues equal). The distinct eigenvalue is more compressive

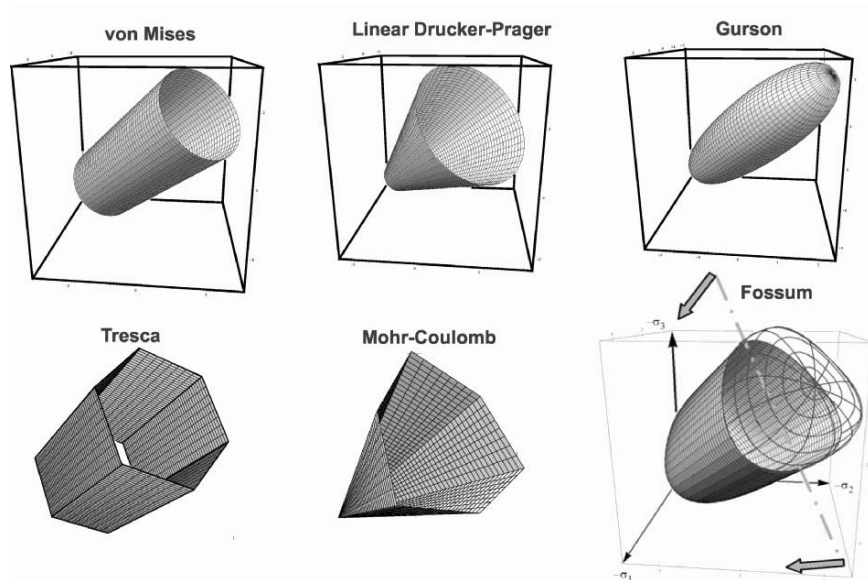


Fig. 6.1. Common isotropic yield surfaces. Von Mises and Drucker–Prager models are often used for metals. Gurson’s function [27], and others like it, are used for porous media. Tresca and Mohr–Coulomb [10] models approximate the yield threshold for brittle media. Fossium’s model [22], and others like it, combine these features to model realistic geological media

than the double eigenvalue for TXC, and less compressive for TXE. Plate-slap and Kolsky bar shock data give information about the TXC yield threshold, whereas spall experiments identify the TXE failure point. Biaxial extension (BXE) and biaxial compression (BXC) are special cases of TXC and TXE, respectively, although the adjective “biaxial” is often used only when the distinct eigenvalue is zero. The adjective “uniaxial” is typically used when the repeated eigenvalue (lateral stress) is zero.

Lode invariants can be determined without having to first compute mechanics invariants. They can be found directly from a stress tensor σ via

$$z = \frac{1}{\sqrt{3}} \text{tr} \sigma, \quad r = \|\mathbf{S}\|, \quad \sin 3\theta = 3\sqrt{6} \det \hat{\mathbf{S}}, \quad (6.13)$$

where “det” denotes the determinant, and $\hat{\mathbf{S}}$ is a unit tensor in the direction of the stress deviator \mathbf{S} . Just as the mechanics invariants (I_1, J_2, J_3) were intimately related to three tensors ($\mathbf{I}, \mathbf{S}, \mathbf{T}$), the Lode invariants are associated with three unit tensors ($\mathbf{E}_r, \mathbf{E}_\theta, \mathbf{E}_z$), analogous to cylindrical base vectors, defined

$$\mathbf{E}_r \equiv \hat{\mathbf{S}}, \quad \mathbf{E}_\theta = \frac{\hat{\mathbf{T}} - (\sin 3\theta) \hat{\mathbf{S}}}{\cos 3\theta}, \quad \mathbf{E}_z \equiv \frac{\mathbf{I}}{\|\mathbf{I}\|} = \frac{\mathbf{I}}{\sqrt{3}}. \quad (6.14)$$

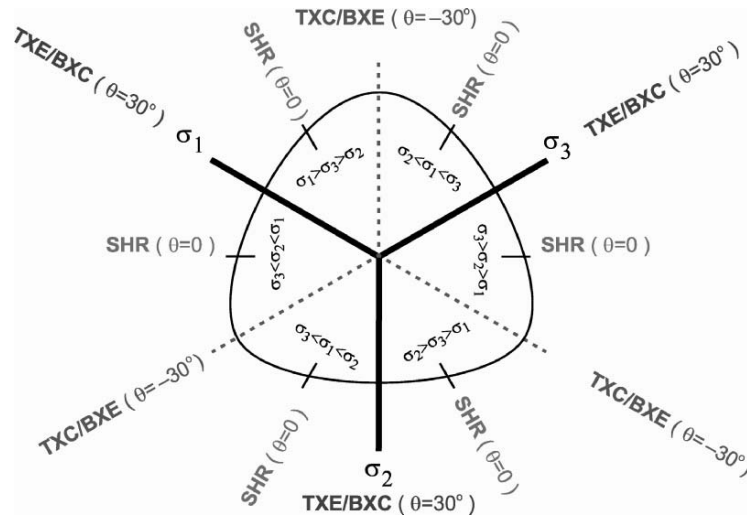


Fig. 6.2. Periodicity of the Lode angle in an octahedral plane

Here

$$\hat{\mathbf{T}} \equiv \frac{\mathbf{T}}{\|\mathbf{T}\|} = \frac{\sqrt{6}\mathbf{T}}{r^2} = \sqrt{6} \left[\hat{\mathbf{S}}^2 - \frac{1}{3}\mathbf{I} \right] = \sqrt{6}\mathbf{E}_r^C + \frac{\mathbf{E}_z}{\sqrt{2}}, \quad (6.15)$$

where \mathbf{E}_r^C is the cofactor of \mathbf{E}_r (i.e., matrix of signed minors [5]). These formulas (offered without proof) should *not* be considered self-evident. The divisor $\sqrt{3}$ in the definition of \mathbf{E}_z occurs for the same reason that a $\sqrt{3}$ appears when normalizing the [111] hydrostat vector. As typical for *any* cylindrical coordinate system, \mathbf{E}_r becomes undefined when $r = 0$ (i.e., when the stress is isotropic and therefore has three equal eigenvalues). The tensor \mathbf{E}_θ is analogous to the 3-D angular base vector $\mathbf{e}_\theta = \mathbf{e}_z \times \mathbf{e}_r$; the cofactor operation in (6.15) is somewhat analogous the 3-D vector cross product, which is not defined in 6-D stress space. Unlike an ordinary cylindrical basis, \mathbf{E}_θ becomes undefined when $\cos 3\theta = 0$ (i.e., when the stress is triaxial, and therefore has two equal eigenvalues). The stress may be written in terms of the Lode basis as

$$\boldsymbol{\sigma} = r\mathbf{E}_r + z\mathbf{E}_z. \quad (6.16)$$

When the yield function is expressed in terms of Lode invariants, its gradient is

$$\frac{\partial f}{\partial \boldsymbol{\sigma}} = \frac{\partial f}{\partial r}\mathbf{E}_r + \frac{1}{r}\frac{\partial f}{\partial \theta}\mathbf{E}_\theta + \frac{\partial f}{\partial z}\mathbf{E}_z. \quad (6.17)$$

Any yield function expressed in terms of principal stresses may be converted to a function of Lode invariants via the following coordinate transformations:

$$\text{LOW: } \sigma_L = \frac{z}{\sqrt{3}} - \frac{r}{\sqrt{2}} \left[\cos \theta - \frac{\sin \theta}{\sqrt{3}} \right] \quad (6.18)$$

$$\text{MIDDLE: } \sigma_M = \frac{z}{\sqrt{3}} - \sqrt{\frac{2}{3}} r \sin \theta \quad (6.19)$$

$$\text{HIGH: } \sigma_H = \frac{z}{\sqrt{3}} + \frac{r}{\sqrt{2}} \left[\cos \theta + \frac{\sin \theta}{\sqrt{3}} \right] \quad (6.20)$$

Though presented in the context of stress, these formulas give the *ordered* eigenvalues of *any* real symmetric tensor. This solution differs from similar formulas presented elsewhere [52,88] in that our definition of the Lode angle is zero in shear and our solution emphasizes that the *ordering* of the eigenvalues may be deduced in closed form.

Lode invariants facilitate drawing geometrically accurate cross-sections of a yield surface. A plot of r vs. z (called a *meridional profile* of the yield surface) indicates how strength varies with pressure, but the axes are scaled to make the plot *isomorphic* to stress space, which means that lengths and angles are preserved as illustrated in Fig. 6.3. Because most materials have greater strength under pressure, Fig. 6.3 uses the “overbar” from (6.1) on the abscissas. Being essentially a “side view” of the yield surfaces in Fig. 6.1, the meridional profile is a horizontal line for von Mises and Tresca models, a sloped straight line for Drucker–Prager and Mohr–Coulomb models, and a curved “capped” line for Gurson’s and Fossum’s models.

See Errata
(end of document).

Now consider viewing Fig. 6.1 down the hydrostat rather than from the side. An *octahedral profile* is a constant- z (constant pressure) cross-section of a yield surface. When z is held constant, a yield criterion $f(r, \theta, z) = 0$ may be solved for $r(\theta)$. Recalling that the Lode angle varies only over the range -30° to 30° , a full octahedral profile with the correct 120° rotational and reflective symmetry may be generated by parametrically plotting $y = r(\theta) \sin \theta$ vs. $x = r(\theta) \cos \theta$ in which θ varies over the full range from 0° to 360° and $\theta = \frac{1}{3} \text{ArcSin}(\sin 3\theta)$.

Drucker–Prager yield models (top row of Fig. 6.1) presume that the octahedral yield profile is circular. This means that a material is as strong in TXE as it is in TXC at the same pressure. Real materials, however, are generally

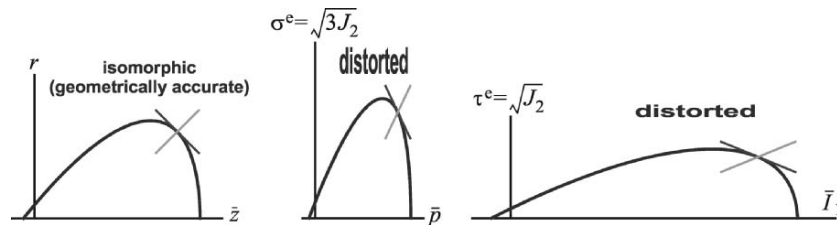


Fig. 6.3. Distortion of a meridional profile when using nonisomorphic stress invariants

weaker in TXE than in TXC, making the distance from the origin to the yield threshold smaller in TXE than in TXC at the same pressure. This well-documented strength difference, which is especially noticeable in geological materials, makes the octahedral yield profile somewhat triangular, as illustrated in Fig. 6.2.

Except where otherwise noted, our upcoming discussion of plasticity theory permits the yield criterion to be *arbitrarily anisotropic*. Myriad yield functions have been developed for *isotropic* materials (common ones are illustrated in Fig. 6.1). If a material is isotropic in its virgin state, it is unlikely to remain isotropic. For computational tractability, many plasticity models have nevertheless ignored deformation-induced anisotropy. Models that support intrinsic or deformation-induced anisotropy typically do so by using an isotropic reference configuration [60] or, somewhat equivalently, transforming the actual stress to an *effective* stress that is used within an *isotropic* plasticity framework. For example, kinematic hardening is modeled by simply replacing all occurrences of the stress deviator \mathbf{S} in an isotropic model with $\mathbf{S} - \boldsymbol{\alpha}$ where $\boldsymbol{\alpha}$ is a history-dependent backstress internal state variable that characterizes the deformation-induced anisotropy associated with the Bauschinger effect. More generally, if $f[\boldsymbol{\sigma}]$ is an *isotropic* yield function, the vast majority of *anisotropic* yield functions [1, 8, 38, 96], dating back to Hill's orthotropy model [29], are expressible in the form $F(\boldsymbol{\sigma}) = f[\mathbb{U} : (\boldsymbol{\sigma} - \boldsymbol{\alpha})]$ in which the fourth-order tensor \mathbb{U} is a “texture” tensor. Care must be taken to ensure that the texture tensor generates a *convex* yield surface. Calibrating a texture model from experimental data can be extraordinarily difficult because the required load paths are not usually achievable with standard laboratory equipment. Recognizing that a yield surface is the boundary of elastic stresses, Schreyer and Zuo [50, 85] proposed that the texture tensor and the elastic stiffness should share the same eigentensors; this assumption can simplify model calibration and help ensure convexity. Brünig [8] provides a nice review of other effective stress approaches to anisotropic damage evolution.

6.3 Rate-Independent Plasticity

This section reverses the historical development of elastoplasticity theory by summarizing the basic mathematics before describing the physical foundations of the theory. The physical meaning of the equations, their domain of applicability, and several examples are discussed extensively only *after* the governing equations and their solution have been presented.

Elastic Loading. Solution of a plasticity problem always begins with a test elastic stress rate,

$$\dot{\boldsymbol{\sigma}}^{\text{test}} = \mathbb{E} : \dot{\boldsymbol{\varepsilon}} \quad (\dot{\sigma}_{ij}^{\text{test}} = E_{ijkl}\dot{\varepsilon}_{kl}). \quad (6.21)$$

Plasticity theory is distinguished from viscoelasticity and creep in that it assumes that reversible elastic deformation *is possible*. For shock physics codes (which typically do not solve the heat conduction equation), \mathbb{E} is the *isentropic* fourth-order elastic stiffness and E_{ijkl} are its components. Hence, despite appearances, (6.21) is *not* purely mechanical. The linear system in (6.21) may be solved for unknown stress or strain rate components, which are then integrated to obtain a time-varying test solution $\boldsymbol{\sigma}^{\text{test}}$. This test solution is the *actual* solution until the predicted stresses fall outside the yield surface. In other words, $\dot{\boldsymbol{\sigma}} = \dot{\boldsymbol{\sigma}}^{\text{test}}$ as long as $f < 0$ (or $f = 0$ and $\dot{f} \leq 0$), where f is the yield function.

The elasticity equation (6.21), applies for arbitrary *anisotropic nonlinear* elasticity. The tangent stiffness of an isotropic material will be itself isotropic if and only if the shear modulus G is constant. The tangent bulk modulus K may vary arbitrarily as determined from an EOS. For these conditions,

$$\dot{\boldsymbol{\sigma}}^{\text{test}} = 2G\dot{\boldsymbol{\epsilon}}^{\text{d}} + 3K\dot{\boldsymbol{\epsilon}}^{\text{iso}}, \quad (6.22)$$

where $\dot{\boldsymbol{\epsilon}}^{\text{d}}$ is the strain-rate deviator, and $\dot{\boldsymbol{\epsilon}}^{\text{iso}}$ is the isotropic part.

Plastic Loading. Plasticity theory applies when the test elastic stress moves beyond the yield surface. During intervals of plastic loading, the governing equations are

$$\text{Strain rate decomposition:} \quad \dot{\boldsymbol{\epsilon}} = \dot{\boldsymbol{\epsilon}}^{\text{e}} + \dot{\boldsymbol{\epsilon}}^{\text{P}}. \quad (6.23)$$

$$\text{Nonlinear coupled elasticity:} \quad \dot{\boldsymbol{\sigma}} = \mathbb{E} : \dot{\boldsymbol{\epsilon}}^{\text{e}} - \mathbf{Z}\dot{\lambda}. \quad (6.24)$$

$$\text{Flow rule:} \quad \dot{\boldsymbol{\epsilon}}^{\text{P}} = \dot{\lambda}\mathbf{M}. \quad (6.25)$$

$$\text{Consistency:} \quad \mathbf{N} : \dot{\boldsymbol{\sigma}} = H\dot{\lambda}. \quad (6.26)$$

In computational plasticity, the following quantities are presumed known:

- $\dot{\boldsymbol{\epsilon}}$ the total strain rate (the “driving” input)
- \mathbb{E} the fourth-order elastic tangent stiffness tensor
- H the ensemble hardening modulus [defined later in (6.47)]
- \mathbf{Z} the elastic–plastic coupling tensor [defined later in (6.39)]
- \mathbf{N} the unit normal to the yield surface, $\mathbf{N} = \frac{\partial f / \partial \boldsymbol{\sigma}}{\|\partial f / \partial \boldsymbol{\sigma}\|}$
- \mathbf{M} the unit tensor in the direction of the plastic strain rate (see p. 238).

The following are unknown:

- $\dot{\boldsymbol{\sigma}}$ the rate of stress
- $\dot{\boldsymbol{\epsilon}}^{\text{e}}$ the elastic part of the strain rate
- $\dot{\boldsymbol{\epsilon}}^{\text{P}}$ the plastic part of the strain rate
- $\dot{\lambda}$ the “consistency parameter” (magnitude of the plastic strain rate).

Equations (6.23) and (6.25) combine to give $\dot{\boldsymbol{\epsilon}}^{\text{e}} = \dot{\boldsymbol{\epsilon}} - \dot{\lambda}\mathbf{M}$, so that (6.24) becomes

$$\dot{\boldsymbol{\sigma}} = \mathbb{E} : (\dot{\boldsymbol{\epsilon}} - \dot{\lambda}\mathbf{M}) - \mathbf{Z}\dot{\lambda}. \quad (6.27)$$

For convenience, we write this in a more compact form

$$\dot{\boldsymbol{\sigma}} = \dot{\boldsymbol{\sigma}}^{\text{trial}} - \mathbf{P}\dot{\lambda}, \quad (6.28)$$

where the “trial elastic stress rate” $\dot{\boldsymbol{\sigma}}^{\text{trial}}$ is defined

$$\dot{\boldsymbol{\sigma}}^{\text{trial}} = \mathbb{E} : \dot{\boldsymbol{\varepsilon}}, \quad (6.29)$$

and \mathbf{P} (which, as explained later in the context of Fig.6.7, is the unique projection direction that must be used in return algorithms) is defined

$$\mathbf{P} \equiv \mathbb{E} : \mathbf{M} + \mathbf{Z}. \quad (6.30)$$

Both $\dot{\boldsymbol{\sigma}}^{\text{trial}}$ and \mathbf{P} may themselves be regarded as known because they are expressed in terms of known quantities. Substituting (6.28) into (6.26) gives

$$\mathbf{N} : (\dot{\boldsymbol{\sigma}}^{\text{trial}} - \mathbf{P}\dot{\lambda}) = H\dot{\lambda}. \quad (6.31)$$

Solving for $\dot{\lambda}$ gives

$$\dot{\lambda} = \frac{\mathbf{N} : \dot{\boldsymbol{\sigma}}^{\text{trial}}}{\mathbf{P} : \mathbf{N} + H}. \quad (6.32)$$

With the consistency parameter known, the other unknowns in the problem may be determined by back substitution. In particular, putting (6.32) back into (6.28) gives the equation governing the stress rate:

$$\boxed{\dot{\boldsymbol{\sigma}} = \dot{\boldsymbol{\sigma}}^{\text{trial}} - \frac{\mathbf{P}(\mathbf{N} : \dot{\boldsymbol{\sigma}}^{\text{trial}})}{\mathbf{P} : \mathbf{N} + H}} \quad \left[\dot{\sigma}_{ij} = \dot{\sigma}_{ij}^{\text{trial}} - \frac{P_{ij}(N_{kl}\dot{\sigma}_{kl}^{\text{trial}})}{P_{rs}N_{rs} + H} \right]. \quad (6.33)$$

The solution in (6.33) lends itself well to physical interpretation and is expressed in a form that is most useful in the *strain-driven* context of finite element codes where $\dot{\boldsymbol{\sigma}}^{\text{trial}}$ identically equals $\dot{\boldsymbol{\sigma}}^{\text{test}}$ from the elastic phase of the analysis. For fully or partly stress-controlled problems, the list of unknowns changes, and, although (6.33) remains valid, it no longer represents a final solution because $\dot{\boldsymbol{\sigma}}^{\text{trial}}$ can no longer be regarded as known (it is certainly a well-defined *symbol*, but it is constructed, in part, from unknown strain rates). Replacing $\dot{\boldsymbol{\sigma}}^{\text{trial}}$ in (6.33) with its definition in (6.29), the solution in (6.33) may be written in an equivalent form as

$$\boxed{\dot{\boldsymbol{\sigma}} = \mathbb{T} : \dot{\boldsymbol{\varepsilon}}} \quad [\dot{\sigma}_{ij} = T_{ijkl}\dot{\varepsilon}_{kl}]. \quad (6.34)$$

Here, the *plastic tangent stiffness tensor* is

$$\boxed{\mathbb{T} = \mathbb{E} - \frac{1}{\eta}\mathbf{P}\mathbf{Q}} \quad \left[T_{ijkl} = E_{ijkl} - \frac{1}{\eta}P_{ij}Q_{kl} \right], \quad (6.35)$$

See Errata
(end of document).

where

$$\boxed{\mathbf{P} \equiv \mathbf{A} + \mathbf{Z}}, \quad \boxed{\mathbf{A} \equiv \mathbb{E} : \mathbf{M}}, \quad \boxed{\mathbf{Q} = \mathbb{E} : \mathbf{N}}, \quad (6.36)$$

and

$$\boxed{\eta = \mathbf{P} : \mathbf{N} + H}. \quad (6.37)$$

Indicial formulas are given in the list of symbols at the end of the chapter. For fully or partially stress-controlled problems (6.34) is a linear system that may be solved for the unknown strain and stress rates, which are then integrated through time to obtain the material response. Though functionally similar in form, (6.34) and (6.21) are different. One corresponds to an exact differential (no hysteresis), while the other gives an inexact differential, which implies history dependence and hysteresis.

6.3.1 Applicability of the Governing Equations

The governing equations in the previous section apply under the following restrictions (or freedoms) for very broad class of material behavior:

- *Arbitrary elastic anisotropy.* The elastic stiffness tensor may be anisotropic.
- *Nonlinear elasticity.* The stress is a proper, permissibly nonlinear, function of the elastic strain, which makes the stress rate linear with respect to the elastic strain rate.
- *Arbitrary plastic anisotropy.* The yield function may depend on the entire stress tensor (rather than just invariants) as long as the function is convex.
- *Nearly arbitrary hardening or softening.* In addition to depending on stress, the yield function is allowed to also depend on any number of internal state variables (ISVs), η_1, η_2, \dots , that characterize the material's microstructural state. The yield surface moves when ISVs change. The hardening is "nearly" arbitrary because the ISVs must not change during elastic loading (see p. 239).
- *Admissible yield function.* So that the yield normal may be determined from the yield function gradient, elastic stresses must correspond to negative values of the yield function f and stresses outside the yield surface must correspond to $f > 0$.
- *Local differentiability of the yield function.* The yield surface normal can be defined only at stress states where the yield function is differentiable. At nondifferentiable points, such as the corners on a Tresca hexagon, vertex theory [40, 56, 70, 89] must be used.
- *Rate independence.* A constitutive model is rate independent if multiplying the strain rate $\dot{\boldsymbol{\epsilon}}$ by an arbitrary positive scalar α will produce $\alpha \dot{\boldsymbol{\sigma}}$ as the predicted stress rate. This idealization plays a pivotal role on p. 255 where we generalize the theory to include rate effects.
- *Rate independence of the plastic strain rate "direction".* The total strain rate is presumed to influence only the *magnitude* $\dot{\lambda}$ of the plastic strain

rate tensor $\dot{\boldsymbol{\epsilon}}^P$. Though rarely validated experimentally, the plastic strain rate *direction* \mathbf{M} is routinely presumed to depend only on the material state, not its rate.

- *Arbitrary ISV coupling of the elastic properties to the plastic flow.* For hardening or softening plasticity where the yield surface changes upon changes of the ISVs, it stands to reason that the elastic properties, which are also tied to the microstructure, might change as well. If, for example, porosity is an ISV, then not only might the yield surface expand (increasing material strength) upon pore collapse, but the material is also likely to become elastically stiffer. Elastic–plastic coupling corresponds to a nonzero \mathbf{Z} tensor in (6.24) (see p. 237).
- *Work conjugate stress and strain definitions.* Plasticity algorithms typically operate internally with alternative stress–strain definitions, but their final results are usually transformed back to more conventional stress and strain measures. In terms of Cauchy stress $\boldsymbol{\Sigma}$ (i.e., the “usual” stress familiar to most engineers), the work rate per unit mass required to deform a material is $J\boldsymbol{\Sigma} : \mathbf{D}$ where J is the Jacobian of the deformation (current volume divided by initial volume) and \mathbf{D} is the symmetric part of the velocity gradient. Demanding that the alternative stress $\boldsymbol{\sigma}$ and strain $\boldsymbol{\epsilon}$ be work conjugate means that $\boldsymbol{\sigma} : \dot{\boldsymbol{\epsilon}} = J\boldsymbol{\Sigma} : \mathbf{D}$.
- *Stress and strain definitions that permit the use of true rates rather than corotational rates.* The principle of material frame indifference requires that a material model must predict consistent results when applied to two deformations that are identical to each other aside from a rigid motion. Plasticity models that are cast in a spatial frame will involve so-called corotational rates, requiring computationally expensive extra steps to convert corotational rates to true rates before integration and to update material directions (such as fiber orientations). On the other hand, material models that are phrased in terms of a nonrotating reference material configuration suffer few of these drawbacks, and the rates that appear in these formulations are true rates from the outset. Before calling the model, the host finite-element code must transform input to the reference configuration and then transform the output back to the spatial frame. This strategy can, by the way, significantly improve accuracy for problems involving massive rotations (e.g., turbine blades) [73].
- *The formulation must allow elastic–plastic decomposition of the total strain rate.* While some stress–strain definitions might satisfy all of the restrictions cited so far, they might not allow the total strain rate to be decomposed into elastic plus plastic parts, which was a fundamental assumption in (6.23).

Small errors in driving strain can produce massive errors in predicted stress. Though not the focus of this chapter, stress and strain definitions, as well as frame indifference, are clearly important topics about which literally thousands of papers have been written [45, 74, 83, 104].

6.3.2 Discussion of the Governing Equations

Decomposition of the total strain rate into elastic and plastic parts in (6.23) follows from the observation that plastic flow induces a residual size and/or shape change (plastic strain) even after loads are removed. The elastic strain rate, which adds to the plastic strain rate, is the recoverable part of the total strain rate.

During elastic loading (when $\dot{\lambda} = 0$, $\dot{\boldsymbol{\varepsilon}}^p = \mathbf{0}$, and therefore $\dot{\boldsymbol{\varepsilon}} = \dot{\boldsymbol{\varepsilon}}^e$), the stress is a function of the strain as well as material properties, such as the *unloaded* porosity, that do not change during elastic loading (yes, porosity changes during elastic loading, but it returns to its *unloaded* value upon removal of the load). During *plastic* loading (when $\dot{\lambda} \neq 0$), some of these material properties that were formerly *implicit constants* in the elasticity model become *explicit variables* during plastic loading (e.g., pores can irreversibly collapse). Poroelastic–plastic coupling has been used here as an example, but plastic flow can also affect elastic properties via thermoelastic–plastic coupling (see p. 242), chemelastic–plastic [86] coupling, and/or kinematic coupling (in which plastic loading makes the origin of stress space no longer reside within the yield surface, necessitating a change in the elastic reference configuration [7]). Applying a principle of equipresence, any internal state variable (ISV) that can affect the yield surface might also affect the elastic response. Consequently, rather than regarding stress to be simply a function of elastic strain, a more general formulation allows it to additionally depend on the ISVs η_1, η_2, \dots . By the chain rule, the rate of stress is then

$$\dot{\boldsymbol{\sigma}} = \frac{\partial \boldsymbol{\sigma}}{\partial \boldsymbol{\varepsilon}^e} : \dot{\boldsymbol{\varepsilon}}^e + \frac{\partial \boldsymbol{\sigma}}{\partial \eta_1} \dot{\eta}_1 + \frac{\partial \boldsymbol{\sigma}}{\partial \eta_2} \dot{\eta}_2 + \dots \quad (6.38)$$

As discussed later, rates of ISVs are typically presumed expressible in the form $\dot{\eta}_k = h_k \dot{\lambda}$, where $\dot{\lambda}$ is the plastic consistency parameter (magnitude of the plastic strain rate) and h_k is an “ISV modulus” material state function (determined experimentally or through microphysical considerations). When the ISVs are presumed to vary in this way, substituting $\dot{\eta}_k = h_k \dot{\lambda}$ into (6.38) gives the ISV-dependent generalized Hooke’s law cited in (6.24), in which

$$E_{ijkl} = \frac{\partial \sigma_{ij}}{\partial \varepsilon_{kl}^e} \quad \text{and} \quad \mathbf{Z} = - \left(\frac{\partial \boldsymbol{\sigma}}{\partial \eta_1} h_1 + \frac{\partial \boldsymbol{\sigma}}{\partial \eta_2} h_2 + \dots \right) \quad (6.39)$$

Elastic–plastic coupling can result from changes in micromorphology or from other sources. In the first category, consider the influence of porosity ϕ (= void volume fraction) on elastic properties. If pores collapse under plastic loading, the elastic response usually stiffens. Consider, for example, the following idealized model [6, 106] for the elastic shear and bulk modulus of a porous material [38, 46, 87]:

$$\frac{G}{G_m} = (1 + \gamma_m \psi)^{-1} \quad \text{where} \quad \gamma_m = \frac{5(4G_m + 3K_m)}{8G_m + 9K_m}, \quad (6.40)$$

238 R.M. Brannon

$$\frac{K}{K_m} = (1 + \kappa_m \psi)^{-1} \quad \text{where} \quad \kappa_m = \frac{4G_m + 3K_m}{4G_m}. \quad (6.41)$$

Here, G_m and K_m are the shear and bulk moduli of the matrix material, and

$$\psi = \frac{\phi}{1-\phi} \approx \phi \text{ if } \phi \ll 1 \quad (6.42)$$

Recognizing ϕ to be an ISV, using these formulas in Hooke's law allows one to compute the derivative $\partial \boldsymbol{\sigma} / \partial \phi$ needed in (6.39). Combining this derivative with the porosity hardening rule (presented later in (6.49)), the elastic-plastic coupling tensor eventually reduces to

$$\mathbf{Z} = (1 + \psi) \left(\frac{\gamma_m}{1 + \gamma_m \psi} \mathbf{S} + \frac{\kappa_m p}{1 + \kappa_m \psi} \mathbf{I} \right) \text{tr} \mathbf{M}, \quad (6.43)$$

where \mathbf{S} is the stress deviator and p is the mean stress (negative of pressure).

Of all the variables that appear in the governing equations, the plastic flow direction \mathbf{M} in (6.25) is most shrouded in mystery, or at least ongoing debate. Early observations of plasticity revealed that, for unconstrained uniaxial tension, a metal can support a certain level of load, after which strain continues to increase without a significant increase in load. This behavior, which is similar to the “Jenkins” element (spring and friction element connected in series) in Fig. 6.4, is well explained through dislocation slip theory. When there are multiple slip planes, the onset of slip depends on the loading direction, which therefore implies existence of a yield surface, and it can be shown in this context that the *direction* of plastic strain rate will be normal to the yield surface ($\mathbf{M} = \mathbf{N}$). Even simple 2-D systems, like the one in Fig. 6.4, that are constructed from multiple Jenkins elements have “yield” surfaces [the diamond-shaped domain in (P_1, P_2) “stress” space] and obey plastic normality ($\mathbf{M} = \mathbf{N}$) with respect to the work conjugate “strains” (Δ_1, Δ_2) . As discussed on p. 250, plastic normality seems essential from a thermodynamics perspective. Nonetheless, many researchers, especially in the geomechanics community, have reported that nonnormality, $\mathbf{M} \neq \mathbf{N}$ (also called *nonassociativity* because the flow direction is not associated with the yield surface), is required to obtain good agreement with experimental data [43, 62].

In quasistatic geomechanics as well as high-rate impact problems [103], a normality rule is usually claimed to predict larger permanent volume changes than exhibited in the data, and “frictional effects” are often nebulously cited as the cause [64]. However, the unquestionably frictional system in Fig. 6.4 can be easily shown to obey a normality rule, so friction cannot per se be the sole cause of apparent non-normality. Lacking precise *materials science* justifications for nonnormality (along with a proof of thermodynamic admissibility), we leave the flow direction \mathbf{M} undefined. See p. 250 for further discussion.

We have now completed a discussion of the physical meaning of all of the rate-independent plasticity equations except the last one, (6.26). Continued yield requires that the stress must remain on the yield surface throughout

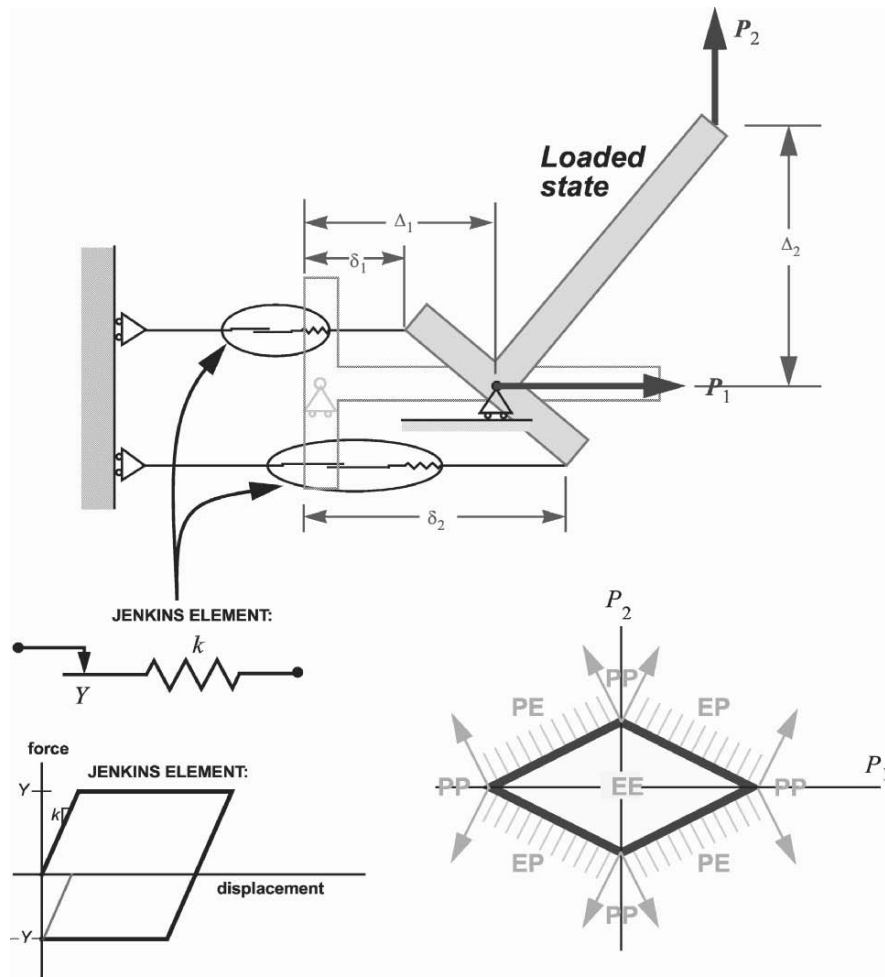


Fig. 6.4. Jenkins element (lower-left) and a 2-D structure containing internal Jenkins elements. *Arrows* normal to the “yield surface” indicate the direction of plastic flow. Labels indicate whether one or both Jenkins elements are responding elastically (E) or plastically (P)

a plastic loading interval. In other words, not only must the yield function $f(\boldsymbol{\sigma}, \eta_1, \eta_2, \dots)$ be zero, its *rate* must also be zero:

$$\dot{f} = \frac{\partial f}{\partial \boldsymbol{\sigma}} : \dot{\boldsymbol{\sigma}} + \frac{\partial f}{\partial \eta_1} \dot{\eta}_1 + \frac{\partial f}{\partial \eta_2} \dot{\eta}_2 + \dots = 0. \quad (6.44)$$

Plasticity theory is distinguished from viscoelasticity and creep in that it supports the approximation that is *possible* for a material to respond elastically (producing no irreversible structural changes in the material). During elastic loading, the yield surface will not move. Therefore, ISVs are almost always

selected so that they themselves do not change during elastic loading. For example, rather than using the current *loaded* porosity (which varies with stress), the *unloaded* porosity is used as an ISV so that it will not vary during elastic loading. Consistent with the assumption that ISVs can change only during plastic loading, their rates are typically governed by an evolution law of the form

$$\dot{\eta}_k = h_k \dot{\lambda}, \quad (6.45)$$

where $\dot{\lambda}$ is the consistency parameter (magnitude of the plastic strain rate) and h_k is the ISV modulus, which must be determined from experiment or microphysical considerations (as clarified in upcoming examples). In general, when a material is deforming plastically, all of the ISVs will change simultaneously. Because the yield surface depends on the ISVs, it will move in stress space as well. Substituting (6.45) into (6.44) gives the result

See Errata

(end of document).

$$\frac{\partial f}{\partial \boldsymbol{\sigma}} : \dot{\boldsymbol{\sigma}} = - \left(\frac{\partial f}{\partial \eta_1} h_1 + \frac{\partial f}{\partial \eta_2} h_2 + \dots \right). \quad (6.46)$$

Dividing both sides by $\|\partial f / \partial \boldsymbol{\sigma}\|$ gives the consistency condition in (6.26) where

$$\mathbf{N} = \frac{\partial f / \partial \boldsymbol{\sigma}}{\|\partial f / \partial \boldsymbol{\sigma}\|} \quad \text{and} \quad H \equiv \frac{- \left(\frac{\partial f}{\partial \eta_1} h_1 + \frac{\partial f}{\partial \eta_2} h_2 + \dots \right)}{\|\partial f / \partial \boldsymbol{\sigma}\|}. \quad (6.47)$$

Dividing by the magnitude of the yield gradient is essential to obtain a physically meaningful (unique) ensemble hardening modulus H that is unaffected by nonuniqueness of yield functions.

Classical nonhardening rate-independent plasticity theory presumes that the yield surface is immovable. Hardening theory (which phenomenologically accounts for dislocation pileups or other changes in micromorphology) permits the yield surface to grow and/or translate, permitting initially inadmissible stress states to be realizable under sufficient continued loading. Softening theory (which, for example, accounts for material weakening arising from microflaw generation and/or dissipative heating) permits the yield surface to shrink. The ensemble hardening modulus H quantifies the combined effect of all ISVs changing simultaneously, resulting in movement of the yield surface. Knowing that the ensemble hardening modulus H follows from the requirement (6.38) that the stress must “keep up” with the moving yield surface during plastic intervals, the consistency condition in (6.26) now has a clear interpretation. Geometrically, $\mathbf{N} : \dot{\boldsymbol{\sigma}}$ is the stress “velocity” in the direction of yield surface normal. Hence, because the stress is “keeping up” with the yield surface, the right-hand side of (6.26) represents the local outward velocity of the yield surface. Being the magnitude of the plastic strain rate, $\dot{\lambda}$ is always positive. Therefore, $H > 0$ corresponds to *hardening*, whereas $H < 0$ corresponds to *softening* (negative hardening). Incidentally, softening can occur *before* a stress–strain plot has a zero slope.

This concludes our outline of the physical meaning of the equations that govern rate-independent plasticity. Further insights can be gained by interpreting the equations in the context of *strain-based* plasticity [7] rather than the more conventional (but equivalent) stress-based plasticity discussed here. Before interpreting the *solution* of the plasticity equations, we now give some examples that clarify the meaning of an ISV modulus h_k .

Hardening Example: Poroplasticity

A porous material can exhibit permanent volume changes as a result of pore collapse. If the matrix material is plastically incompressible, then permanent volume changes observed on the macroscale must result from a change in porosity. Hence, the microscale variable ϕ (porosity) can be related to the macroscopically observable plastic strain [63]. Specifically, assuming plastic incompressibility of the matrix material implies that

$$\dot{\phi} = (1 - \phi) \text{tr} \dot{\boldsymbol{\epsilon}}^P, \tag{6.48}$$

or, since $\dot{\boldsymbol{\epsilon}}^P = \dot{\lambda} \mathbf{M}$, the *microphysically derived* hardening law is

$$\dot{\phi} = h_\phi \dot{\lambda}, \quad \text{where } h_\phi = (1 - \phi) \text{tr} \mathbf{M} \tag{6.49}$$

To illustrate an *empirically based* hardening law, consider Fig. 6.5. As the solid aluminum is deformed plastically, its uniaxial yield stress Y increases. An ISV modulus for Y is needed because (1) the yield criterion presumably depends on Y and (2) Y varies in response to plastic flow. A phenomenological model presumes a power-law relationship,

$$Y = Y_0 + k (\gamma^P)^m, \tag{6.50}$$

where Y_0 is the initial strength, k and m are fitting parameters, and $\boldsymbol{\gamma}^P$ is the effective distortional plastic strain defined in the symbol definitions list on page 270. Taking the rate of (6.50) and substituting the definition of $\dot{\gamma}^P$ allows the ISV rate to be written in the form required in (6.45):

$$\dot{Y} = h_Y \dot{\lambda}, \quad \text{where } h_Y = mk [(Y - Y_0)/k]^{(m-1)/m} \sqrt{\mathbf{M}^d : \mathbf{M}^d}. \tag{6.51}$$

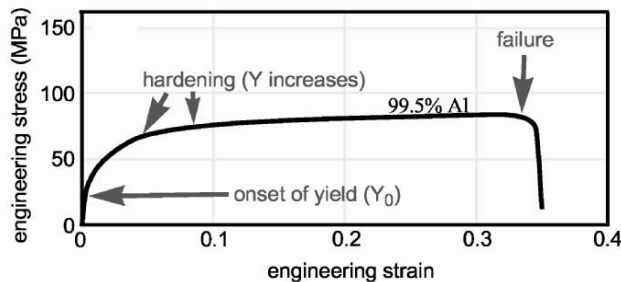


Fig. 6.5. Hardening (increasing yield strength) for aluminum

Equation (6.50) is a strain hardening model. When additionally considering porosity, work hardening (in which γ^p is replaced by plastic work) may be more appropriate because it would allow matrix hardening even under hydrostatic loading.

Given *individual* porosity and hardening ISV moduli (h_ϕ and h_Y), like those in (6.49) and (6.51), the ensemble hardening modulus H for a porous composite can be determined if it is known how the *yield function* depends on the matrix strength Y and porosity ϕ . Though numerous yield functions have been offered for porous media [21, 48, 67, 72, 107], the quintessential example is Gurson's function [27] (which is actually only an upper bound):

$$f = \frac{3J_2}{Y^2} + 2\phi \cosh\left(\frac{2I_1}{Y}\right) - [1 + \phi^2]. \quad (6.52)$$

Derivatives of this yield function with respect to the ISVs, Y and ϕ , can be readily computed, and (6.1) may be used to obtain the yield gradient. Then the ensemble hardening modulus for this porous composite is determined from (6.47):

$$H = \frac{-\left(\frac{\partial f}{\partial Y} h_Y + \frac{\partial f}{\partial \phi} h_\phi\right)}{\|\partial f / \partial \boldsymbol{\sigma}\|}. \quad (6.53)$$

In general, both Y and ϕ will change *simultaneously*, possibly with competitive effects. The sign of H indicates whether the net strength increases or decreases.

Coupling and Hardening Example: Thermoelastoplasticity

The vast majority of shock-physics codes do not solve the heat conduction equation, which (though debatable [101]) seems reasonable because high-rate processes lack sufficient time to conduct heat. Consequently, all problems solved in these codes must be adiabatic. "Adiabatic," which means no heat flow, is *not* synonymous with "isentropic" except during reversible processes such as elastic loading. During adiabatic plastic loading, many plasticity models presume that entropy, s , evolves according to

$$T\dot{s} = \frac{1}{\rho} \boldsymbol{\sigma} : \dot{\boldsymbol{\epsilon}}^p, \quad (6.54)$$

where T is temperature and ρ is mass density (or reference density when reference stress-strain measures are used). Because entropy cannot change during adiabatic *elastic* loading, the entropy s can be formally regarded as an internal state variable for which (6.54) gives an evolution equation of the form required in (6.45). Namely,

$$\dot{s} = h_s \dot{\lambda}, \quad \text{where} \quad h_s = \frac{1}{\rho T} \boldsymbol{\sigma} : \mathbf{M}. \quad (6.55)$$

When thermal effects are included, the elastic Hooke's law is replaced by a *thermoelastic* constitutive law in which stress depends not only on the elastic

strain, but also on the entropy. Hence, the ISV-dependent (thermoelastic) Hooke's law must be of the form in (6.24) for which (6.39) requires

$$\mathbb{E} \equiv \frac{\partial \boldsymbol{\sigma}}{\partial \boldsymbol{\varepsilon}^e} \quad \text{and} \quad \mathbf{Z} \equiv - \left(\frac{\partial \boldsymbol{\sigma}}{\partial s} \right) h_s. \quad (6.56)$$

The partial derivative $\partial \boldsymbol{\sigma} / \partial s$, in which elastic strain is held constant, can be written

$$\frac{\partial \boldsymbol{\sigma}}{\partial s} = -\rho T \boldsymbol{\Gamma}, \quad (6.57)$$

where $\boldsymbol{\Gamma}$ is the Grüneisen tensor. For an *isotropic* material, $\boldsymbol{\Gamma} = \gamma \mathbf{I}$, where γ is the Grüneisen parameter, which appears frequently in shock-physics analyses (and whose value is often found in material property tables). Substituting (6.55) and (6.57) into (6.56), the thermoelastic–plastic coupling tensor is

$$\mathbf{Z} = \boldsymbol{\Gamma} (\boldsymbol{\sigma} : \mathbf{M}). \quad (6.58)$$

Thermoelastic–plastic coupling (in particular its tendency to produce apparent nonnormality) was first noted by Tvergaard [97]. Properly incorporating thermoelastic–plastic coupling with other features in a plasticity model naturally requires a more sophisticated analysis than the simple example presented here [39, 44, 58, 80]. For example, (6.54) requires revision when only a *portion* of the plastic work rate is dissipative (typically 90% for solid metals); this behavior is usually ascribed to “ratcheting” (see p. 252).

6.3.3 Interpreting and Integrating the Stress Rate

Numerically integrating the stress rate in (6.33) over a period of plastic loading is facilitated by first interpreting the solution geometrically. Consider a simple nonhardening idealization where the yield surface is fixed in stress space (no ISVs). Then both the hardening modulus H and the elastic–plastic coupling tensor \mathbf{Z} are zero, and (6.33) reduces to

$$\dot{\boldsymbol{\sigma}} = \dot{\boldsymbol{\sigma}}^{\text{trial}} - \frac{\mathbf{A} (\mathbf{N} : \dot{\boldsymbol{\sigma}}^{\text{trial}})}{\mathbf{A} : \mathbf{N}}, \quad (6.59)$$

where

$$\mathbf{A} \equiv \mathbb{E} : \mathbf{M}. \quad (6.60)$$

As discussed on page 227, second-order symmetric tensors are also 6-D vectors for which the double dot product plays a role analogous to the single vector dot product for ordinary 3-D vectors. Therefore, to interpret (6.59) *geometrically*, consider the following similar operation on ordinary 3-D vectors:

$$P(\mathbf{x}) = \mathbf{x} - \frac{\mathbf{a} (\mathbf{n} \cdot \mathbf{x})}{\mathbf{a} \cdot \mathbf{n}}. \quad (6.61)$$

This operation obliquely projects the vector \mathbf{x} onto a plane whose unit normal is \mathbf{n} , essentially giving the “shadow” cast by \mathbf{x} in the late afternoon sun. The “light rays” (properly called level sets) are parallel to \mathbf{a} . The magnitude of \mathbf{a} is

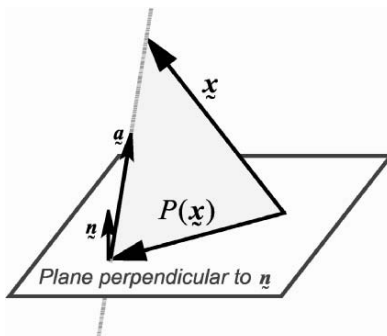


Fig. 6.6. Oblique projection

inconsequential; all that matters is its orientation. The projection is “closest point” (high noon) if and only if \mathbf{a} is parallel to \mathbf{n} .

The plasticity solution in (6.59) is structured like (6.61), and its geometrical interpretation is identical. The yield normal \mathbf{N} defines the target surface for the projection. Because \mathbf{N} is normal to the yield surface, (6.39) states that the *actual* stress rate is an oblique projection of the *trial* stress rate onto the yield surface. The projection is oblique because, in general, \mathbf{A} is not a multiple of \mathbf{N} —not even for associative plasticity where $\mathbf{M} = \mathbf{N}$. The projection direction is not generally aligned with the plastic flow direction either. The projection direction is parallel to the plastic flow direction if and only if the plastic flow direction is an eigentensor of the elastic stiffness. For isotropic linear elasticity, the flow and projection directions will be parallel if one assumes plastic incompressibility. However, for plastically compressible materials such as porous media, these tensors point in different directions.

The 3-D geometrical analog of the 6-D stress rate solution in (6.59) helps formulate extremely efficient elastic-predictor/plastic-corrector return algorithms [76, 102] for nonhardening plasticity. Numerical evaluation of elasto-plasticity equations is complicated by the fact that one set of equations applies during elastic loading, while a different set applies during plastic loading. A time step that begins elastic *but ends plastic* could be problematic were it not for the fact that the actual stress rate during (nonhardening) plastic loading is a projection of the trial stress rate. Working out the first-order integration of the stress rate reveals that the updated stress $\boldsymbol{\sigma}^{\text{new}}$ has the same projection as the trial elastic stress $\boldsymbol{\sigma}^{\text{trial}}$ *regardless of whether the time step was partially elastic*. Hence, there exists a scalar Γ such that

$$\boldsymbol{\sigma}^{\text{new}} = \boldsymbol{\sigma}^{\text{trial}} - \Gamma \mathbf{A}. \quad (6.62)$$

The scalar Γ (which, incidentally, equals the magnitude of the plastic strain increment) is determined by requiring the updated stress to be on the yield surface. In other words, Γ is the solution to

$$f(\boldsymbol{\sigma}^{\text{trial}} - \Gamma \mathbf{A}) = 0. \quad (6.63)$$

In this scalar-valued equation, the only unknown, Γ , may be found by secant or Newton iteration. For simple models (such as nonhardening von Mises plasticity), the solution can be found in closed form. Once known, Γ may be substituted into (6.62) to update the stress.

Numerical Integration for Hardening Plasticity

When the yield surface evolves in response to changes in the ISVs, the general solution in (6.33) must be used. Namely,

$$\dot{\boldsymbol{\sigma}} = \dot{\boldsymbol{\sigma}}^{\text{trial}} - \frac{\mathbf{P}(\mathbf{N} : \dot{\boldsymbol{\sigma}}^{\text{trial}})}{\mathbf{P} : \mathbf{N} + H}, \quad (6.64)$$

Comparing with the nonhardening solution in (6.59), not only is there now a scalar H in the denominator, but the tensor \mathbf{P} also differs from \mathbf{A} whenever elastic properties are affected by plastic flow. Unlike (6.59), the solution in (6.64) is *not* a projection of the trial stress rate. However, it is still true that

$$\dot{\boldsymbol{\sigma}} = \dot{\boldsymbol{\sigma}}^{\text{trial}} - \dot{\lambda}\mathbf{P}, \quad \text{where} \quad \dot{\lambda} = \frac{(\mathbf{N} : \dot{\boldsymbol{\sigma}}^{\text{trial}})}{\mathbf{P} : \mathbf{N} + H}. \quad (6.65)$$

Therefore, in a numerical time step (including partly elastic steps), there exists a scalar Γ such that

$$\boldsymbol{\sigma}^{\text{new}} = \boldsymbol{\sigma}^{\text{trial}} - \Gamma\mathbf{P} \quad (6.66)$$

This equation looks like (6.62) except that \mathbf{P} now plays the role formerly played by \mathbf{A} in the nonhardening case. In the nonhardening case, Γ was found by demanding that $\boldsymbol{\sigma}^{\text{new}}$ must be on the stationary (nonhardening) yield surface. Nearly the same condition applies here, but the yield surface to which the trial stress is projected must be the *updated* surface. Updating the yield surface requires updating the ISVs, which requires integrating $\dot{\lambda}$ in (6.66) over the *plastic part* of the time step. Thus, with hardening plasticity, the tremendous algorithmic advantages of predictor–corrector return algorithms are less apparent because the duration of the plastic part of the time step, Δt^{P} , must be determined either *explicitly* (so that (6.65) may be applied to find the increment $\Gamma \equiv \dot{\lambda}\Delta t^{\text{P}}$ needed to update the ISVs) or *implicitly* through iterations for Γ that include evolution of the location of the yield surface.

When using iterative methods to determine Γ , a good (first-order accurate) approximation to the solution is

$$\Gamma = \Gamma_0 \left(\frac{\mathbf{P} : \mathbf{N}}{\mathbf{P} : \mathbf{N} + H} \right), \quad (6.67)$$

where, generalizing (6.63) to now include coupling and hardening effects, Γ_0 is the solution to

$$f(\boldsymbol{\sigma}^{\text{trial}} - \Gamma_0\mathbf{P}, \eta_1^0, \eta_2^0, \dots) = 0. \quad (6.68)$$

Here, η_k^0 are the known values of the ISVs at the beginning of the time step. Recalling that $\mathbf{N} : \dot{\boldsymbol{\sigma}}$ represents the normal velocity of the yield surface (so that, referring to (6.26), $H\dot{\lambda}\Delta t^P = H\Gamma$ is the incremental normal displacement), the geometrical interpretation of (6.67) is illustrated in Fig. 6.7. Of course, once Γ is determined, the stress is updated by using (6.66), and the internal state variables are updated by $\eta_k^{\text{new}} = \eta_k^0 + h_k\Gamma$. The increment in the equivalent total plastic strain is updated according to

$$\Delta e^P = \dot{\lambda}\Delta t^P = \Gamma. \tag{6.69}$$

This result shows that the projection distance factor Γ has a compelling physical interpretation: it is the magnitude of the total plastic strain increment.

In the literature, inordinate attention has been paid to high-order numerical accuracy, while the far more essential need to verify *consistency* is virtually ignored. An algorithm is “consistent” if it is at least first-order accurate. In the limit as the time step goes to zero, the projection direction *must* equal the value of \mathbf{P} at the onset of plasticity. The fact that the projection *distance* Γ becomes smaller as the time step decreases might lead one to incorrectly surmise that the projection *direction* should be inconsequential as the time step goes to zero. However, any projection direction other than \mathbf{P} results in a first-order error in the stress rate, which violates consistency (the predictor–corrector algorithm will converge—but to the wrong result, which leads to incorrect model parameter calibrations when using the flawed code).

A widespread misconception that the return direction is parallel to the plastic strain rate is perhaps perpetuated by publications whose *equations* properly indicate that the return direction is parallel to the stiffness acting on the flow direction but whose *illustrations* (such as “Fig. 1” in [65]) incorrectly show only the flow direction without the transformation. They show \mathbf{M} where they should show \mathbf{P} , and they use the phrase “closest-point” projection for what is, in fact, an oblique projection. This problem is rectified to some extent by the emphasis of Simo and Hughes [88] (in their “Figs. 3–8”) that the projection for associative plasticity is closest point *with respect to the metric defined by the elastic stiffness (energy norm)*. However,

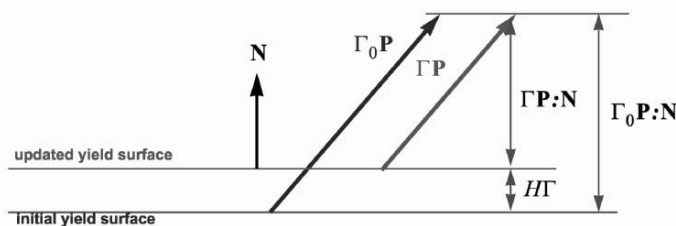


Fig. 6.7. Using the plastic strain increment (Γ_0) that would apply if not hardening to determine the actual increment (Γ) with hardening

this still means it is oblique with respect to an ordinary norm in stress space, as shown in Fig. 6.8, which depicts a typical meridional yield profile for a porous material whose matrix strength is pressure dependent (the Lode radius r is proportional to shear strength and the Lode axial coordinate \bar{z} is proportional to pressure). Proportions in that plot use a Poisson's ratio of $1/3$, making it clear that the proper return direction is *not even approximately* a closest-point trajectory in stress space.

Higher-order integration strategies address the possibility that \mathbf{P} might vary during large plastic time steps. For a fully implicit backward Euler integration (in which the projection direction tensor \mathbf{P} is evaluated at the *end-state*), Simo [89] showed that the plastic integration problem can be transformed into a constrained optimization problem (in which the conditions that differentiate between elastic and plastic flow are mathematically formalized as the “Kuhn–Tucker conditions,” $\{\dot{\lambda}f = 0, \dot{\lambda} \geq 0, f \leq 0\}$). Various studies [42, 65, 84] have verified that the implicit Euler Backward algorithm is stable for J_2 -plasticity as well as for more sophisticated plasticity models (though a recent study [19] claims that significant truncation errors can result when backward Euler schemes are used with kinematic hardening). These and other studies [12, 20, 81, 91] have used “numerical experiments” to demonstrate that results are accurate, but they presume that a converged solution is actually a correct solution (i.e., they fail to demonstrate *consistency*), so these claims of accuracy are really only assertions of high convergence rates, possibly to incorrect results. Incidentally, for linear-elastic three-invariant isotropic yield models, efficiency improvements can be gained through spectral representations of the stresses and strains so that the problem is solved in 3-D principal stress space rather than 6-D stress *tensor* space [4].

In their classical and frequently cited paper about consistent tangent operators for higher-order accuracy, Simo and Taylor [90] emphasize that the tangent stiffness must be obtained by consistent linearization of the stress resulting from the return-mapping algorithm. In the context of an elastic-predictor/plastic-corrector iterative algorithm, this means that, once an iteration cycle has given a new approximation for the final stress state, all of the

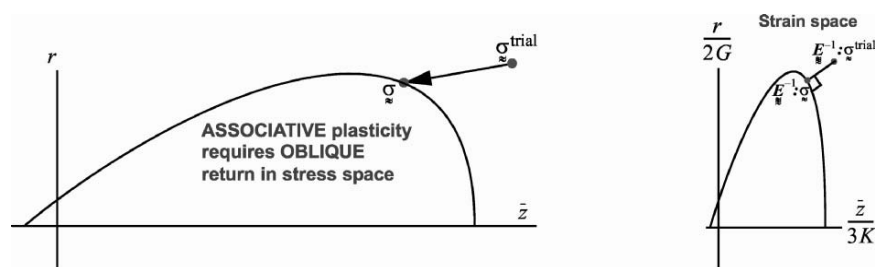


Fig. 6.8. Associative plasticity does not correspond to a closest-point return with respect to an ordinary Euclidean norm in stress space

quantities that appear in the tangent stiffness should be re-evaluated at the new prediction before proceeding with the next iteration. For nonhardening plasticity, the only thing that might change during plastic loading is the tensor \mathbf{A} , but for hardening plasticity re-evaluations of the tangent stiffness must also include updates of the ISVs, and quantities derived from them (H and \mathbf{Z}). In this process, higher-order accuracy is secondary to *consistency* (i.e., correctly performing any *single* iteration by using the correct projection direction, \mathbf{P} not \mathbf{M}). If iterations are performed using an incorrect return direction, then these algorithms will converge (efficiently) *to the wrong result*.

6.4 Nonhardening von Mises (J_2) Plasticity

Von Mises theory (also called Huber–Mises or J_2 plasticity) is supported in virtually all shock-physics codes. Though of limited use for real materials, this model is useful for verifying consistency and accuracy [42, 105] and for performing shake-down calculations. The yield criterion is $J_2 = \tau_y^2$, where τ_y is a material constant (yield in shear). This criterion,

$$\mathbf{S} : \mathbf{S} = 2\tau_y^2, \quad (6.70)$$

describes a cylinder of radius $\sqrt{2}\tau_y$ in stress space (see Fig. 6.1). In numerical calculations, the updated stress deviator \mathbf{S}^{new} is parallel to the trial stress deviator $\mathbf{S}^{\text{trial}}$. Hence, the trial stress deviator is simply scaled down by a multiple that puts the stress on the yield surface (a process known as “radial return”):

$$\mathbf{S}^{\text{new}} = \Psi \mathbf{S}^{\text{trial}} \quad \text{where} \quad \Psi = \sqrt{\frac{2\tau_y^2}{\mathbf{S}^{\text{trial}} : \mathbf{S}^{\text{trial}}}}. \quad (6.71)$$

For von Mises theory, the isotropic parts of the updated and trial stresses are identical ($p^{\text{new}} = p^{\text{trial}}$). Because (6.71) uses the trial stress (at the end of the step), this strategy is sometimes referred to as a backward Euler integration, and it is unconditionally stable. The integration error tensor ($\mathbf{S}^{\text{new}} - \mathbf{S}^{\text{new}_{\text{exact}}}$) is

$$G(\Delta t)^2 \{[\ddot{\gamma}_0 - \mathbf{N}_0(\mathbf{N}_0 : \ddot{\gamma}_0)] - (\mathbf{N}_0 : \dot{\gamma}_0)[\dot{\gamma}_0 - \mathbf{N}_0(\mathbf{N}_0 : \dot{\gamma}_0)]\} + O(\Delta t)^3, \quad (6.72)$$

where G is the shear modulus, $\dot{\gamma}_0$ is the strain rate deviator tensor, $\ddot{\gamma}_0$ is the strain “acceleration”, and \mathbf{N}_0 is a unit tensor in the direction of the stress deviator, all evaluated at the beginning of the step. Suppose the strain rate is constant so that $\ddot{\gamma}_0 = \mathbf{0}$. Then the error in (6.72) evaluates to zero if the strain rate is exactly tangent to the yield surface ($\mathbf{N}_0 : \dot{\gamma}_0 = 0$) or if it points directly against the yield surface [$\dot{\gamma}_0 - \mathbf{N}_0(\mathbf{N}_0 : \dot{\gamma}_0) = \mathbf{0}$]. In these special cases, radial return is at least second-order accurate. In general, however, the method is only first-order accurate because the error in (6.72) is of order

$(\Delta t)^2$. When the strain rate is constant, integration error is most severe when the strain rate forms a 45° angle with the yield surface. True second-order accuracy requires not only the strain rate $\dot{\gamma}_0$, but also the strain “acceleration” $\ddot{\gamma}_0$ which is not typically available in shock-physics codes even though it is undoubtedly large in shock zones. Thus, from a practical standpoint, first-order accuracy is the best one should expect from *any* material model if $\dot{\gamma}_0$ is unavailable.

Of particular interest to the shock-physics community are the special cases of uniaxial stress and uniaxial strain loading. For these problems, the direction of the stress deviator is constant during plastic loading and a radial return von Mises algorithm is *exact* regardless of the time step size. The stress–strain response for nonhardening von Mises plasticity under uniaxial stress and uniaxial strain (assuming isotropic linear elasticity) is as illustrated in Fig. 6.9 where K is the bulk modulus, E is Young’s modulus, and C is the constrained modulus ($C = K + \frac{4}{3}G$). The uniaxial strain yield threshold, $CY/2G$ is often called the “Hugoniot elastic limit (HEL)”. For uniaxial strain, the distance between load and unload lines is $4Y/3$, where $Y = \sqrt{3}\tau_y$ is the strength in uniaxial stress. One must be cautioned, however, that this separation distance will be different for materials whose octahedral profile is noncircular (as is usually the case for brittle materials). Likewise, the separation of load–unload response curves is also affected by pressure sensitivity, which can be pronounced for brittle materials where von Mises theory is grossly inappropriate [11]. This point is reiterated in Fig. 6.10.

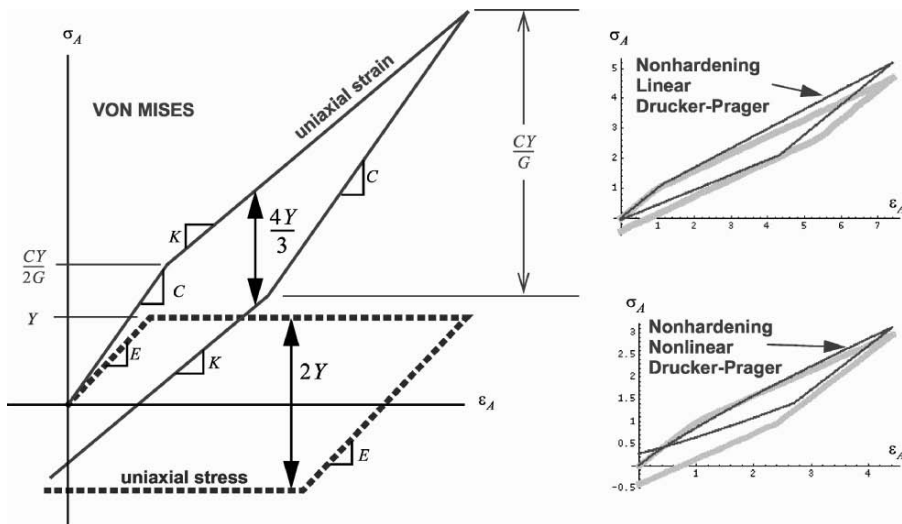


Fig. 6.9. Comparison of uniaxial axial stress loading (*dashed*) with uniaxial strain loading (*solid*) for linear-elastic nonhardening von Mises plasticity. To emphasize that the labels in the first plot apply only for von Mises plasticity, comparisons are shown for different yield models that allow variation of strength with pressure

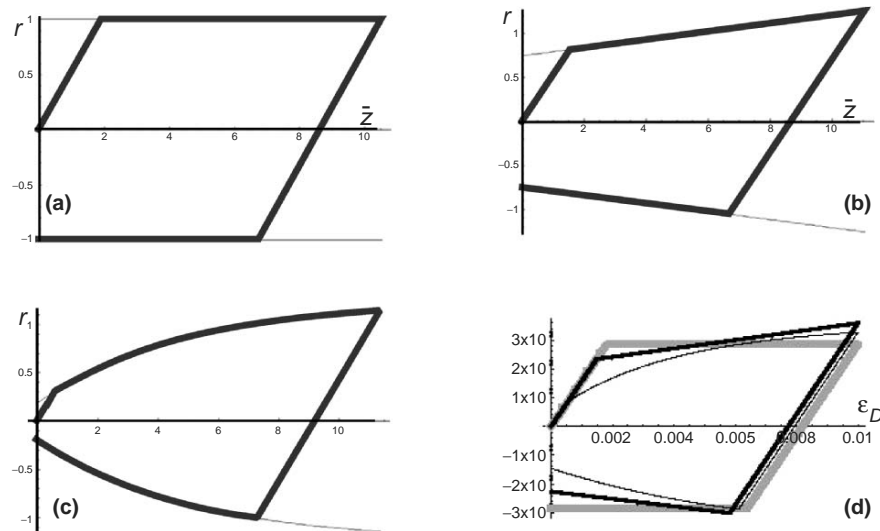


Fig. 6.10. Stress-space trajectories for uniaxial strain loading using *nonhardening* (a) von Mises, (b) linear Drucker–Prager, and (c) nonlinear Drucker–Prager models. Resulting differences in the axial response were shown in Fig.6.9, and (d) in this figure shows distinction in stress difference plots

6.5 Phantom Inelastic Partitioning

Adding advanced features to a plasticity model brings on a host of lurking pitfalls related to physical interpretations of the new terms. This section discusses “phantom inelastic partitioning,” which is a philosophical term conveying the consequences of conflicting physical interpretations of the various parts of observed strain rates (i.e., interpretations that are inconsistent with other researchers’ work against which a model is assessed). Earlier, we decomposed the total strain rate as $\dot{\epsilon} = \dot{\epsilon}^e + \dot{\epsilon}^P$. As advanced constitutive features are incorporated, the strain rate might decompose into something more complicated like

$$\dot{\epsilon} = \dot{\epsilon}^e + \dot{\epsilon}^P + \dot{\epsilon}^t + \dot{\epsilon}^c + \dot{\epsilon}^x, \quad (6.73)$$

where $\dot{\epsilon}^P$ might represent only the strain rate from classical “dislocation-type” plastic flow, while $\dot{\epsilon}^t$, $\dot{\epsilon}^c$, and $\dot{\epsilon}^x$ could be strain rates from a host of other sources, such as phase transformation, elastic–plastic coupling, etc. If a decomposition like (6.73) is forced into the form of a traditional two-term decomposition $\dot{\epsilon} = \dot{\epsilon}^e + \dot{\epsilon}^P$, it must be made very clear whether $\dot{\epsilon}^t$, $\dot{\epsilon}^c$, and $\dot{\epsilon}^x$ are absorbed into $\dot{\epsilon}^e$ or $\dot{\epsilon}^P$. If absorbed into $\dot{\epsilon}^e$, then the equation governing the elastic response will have extra terms like \mathbf{Z} in (6.24). If absorbed into $\dot{\epsilon}^P$, then residual strain is no longer the time integral of $\dot{\epsilon}^P$. Either choice leads to an *apparent* plastic flow direction that differs from the actual flow direction.

For simple work-hardening materials, plastic convexity and normality ($\mathbf{M} = \mathbf{N}$) follow from Drucker's stability postulates [14–16, 54], which are based on phenomenological assumptions about the general character of material response one would expect to observe at the macroscale, regardless of microphysical origins. For hardening *or softening* materials, normality again results from a more general postulate of maximum plastic dissipation put forth in pioneering research efforts [28, 30, 35, 61, 95], as well as countless follow-up studies. A normality law follows from an even more generalized thermodynamics principle of maximum rate of entropy production [80] that supports elastic–plastic coupling by allowing the energy potential and dissipation to depend on internal state variables. *Neglecting elastic–plastic coupling*, Sandler, Rubin, and Pućik [71, 78, 79] demonstrated that a nonnormality rule in a rate-independent local plasticity model allows an infinitesimal perturbation to propagate with unbounded amplitude (i.e., spontaneous motion from a quiescent state), which is a physically unacceptable result that leads to nonuniqueness of dynamic plasticity solutions.

Despite a preponderance of theoretical and anecdotal arguments against it, nonnormality ($\mathbf{M} \neq \mathbf{N}$) is used routinely in plasticity models for the simple reason that it better matches experimental data (especially for geological [100] and porous [57, 92] materials). No such model has (to our knowledge) been proved consistent with thermodynamics for all load paths. Besides validating in domains where data exist, nonassociative models must also be checked for thermodynamically objectionable results under “Sandler–Rubin–Pućik” type loading conditions (where $\dot{\boldsymbol{\sigma}}^{\text{trial}} : \mathbf{N} > 0$ but $\dot{\boldsymbol{\sigma}}^{\text{trial}} : \mathbf{M} < 0$). Experimental studies in this domain are earnestly needed (and could be easily accomplished in confined triaxial tests by loading a material to yield and then methodically studying the effect of changing the loading direction by changing the axial and lateral loads in differing proportions). Sandler, Rubin, and Pućik reasonably suggest that objections to nonnormality might be resolved by including rate dependence. However, the issue might be rooted simply in misassessments of nonnormality.

We define “*phantom inelastic partitioning*” to be any invalid logic or imprecise language applied toward assessing the direction of the plastic/inelastic strain rate or any of its partitions. These errors are flawed reasoning, not necessarily flawed conclusions. Perhaps nonassociativity is truly needed for a particular material, but an issue exists if improper logic is used to *justify* such a conclusion or if the conclusion is at odds with thermodynamics. If an error is related to vague or missing strain rate partitions, then the partitioning analysis cannot be corroborated or disproved by independent researchers. The list below describes sources of phantom inelastic partitioning (especially misassessment of the extent of non-normality) that we have encountered in our daily work with materials modelers, experimentalists, and users of production finite element codes.

- *Erroneous belief that the return direction is parallel to the plastic strain rate.* As discussed on p. 246, the correct direction needed to return a

stress to the yield surface is not discretionary. Incorrectly interpreting the required return direction \mathbf{P} as if it were parallel to \mathbf{M} leads to misassessment of \mathbf{M} .

- *Nonisomorphic depictions of a yield surface.* Figure 6.3 illustrated that the geometrical shape of the yield surface in stress space is preserved only when using Lode coordinates (r, z) in meridional profiles. A line segment that is normal to the yield surface in stress space will be no longer normal to the yield surface in a non-isomorphic plot (such as shear strength vs. pressure), thus producing phantom (false) non-normality where normality actually applies.
- *Stress-dependent internal variables.* On p. 239, we emphasized that internal state variables should be defined such that they change only during plastic loading. If the yield function is written as $F(\boldsymbol{\sigma}, \Phi)$ in which Φ depends on stress (e.g., the actual porosity in a material rather than the unloaded porosity), then the yield normal will be parallel to

$$\frac{\partial F}{\partial \boldsymbol{\sigma}} + \frac{\partial F \partial \Phi}{\partial \Phi \partial \boldsymbol{\sigma}}.$$

Mistakenly comparing the plastic flow direction against $\partial F / \partial \boldsymbol{\sigma}$ can result in misassessments of nonnormality.

- *Erroneous belief that nonmajor-symmetry of the plastic tangent stiffness implies nonassociativity.* In the absence of elastic–plastic coupling, the actual stress rate differs from the trial stress rate by a multiple of \mathbf{A} (where, recall, $A_{ij} = E_{ijkl} M_{kl}$), in which case associativity implies major-symmetry of the plastic tangent stiffness. With elastic–plastic coupling, however, the difference between these stress rates is a multiple of $\mathbf{P} = \mathbf{A} + \mathbf{Z}$, where \mathbf{Z} is the elastic–plastic coupling tensor from (6.39). Mistakenly interpreting \mathbf{P} as if it equals \mathbf{A} can result in phantom nonnormality [51, 97].
- *Ratcheting.* Most continuum plasticity theories presume that the elastic strain goes to zero when loads are released from a small representative volume element. In reality, however, elastic strains (near, e.g., micropores or dislocation pile-ups) can exist at the microscale even after loads are released, much as a ratchet has phantom permanent deformation that properly should be regarded as elastic deformation (recoverable by pressing the “release” button). A theory that accommodates ratcheting would need to decompose the strain rate as $\dot{\boldsymbol{\epsilon}} = \dot{\boldsymbol{\epsilon}}^e + \dot{\boldsymbol{\epsilon}}^p + \dot{\boldsymbol{\epsilon}}^r$, where $\dot{\boldsymbol{\epsilon}}^r$ is the ratcheting strain rate. At the macroscale, the apparent plastic strain rate would equal $\dot{\boldsymbol{\epsilon}}^p + \dot{\boldsymbol{\epsilon}}^r$, but only $\dot{\boldsymbol{\epsilon}}^p$ would be dissipative (entropy generating). For granular materials, ratcheting is likely to be evident even at the mesoscale where shearing across rough surfaces requires uplift (dilatation) to overcome geometrical obstacles. Following a program of triaxial compression with an associative flow rule, the apparent plastic strain is likely to be larger than the actual plastic strain with ratcheting removed.
- *Erroneous assessment of the relative magnitude of elastic and plastic strains rates.* In early metals plasticity research, the deviatoric part of the elastic strain rate was often presumed small compared to the plastic

strain rate. Though this assumption is justified for load paths that push directly against the yield surface, it is not appropriate for significantly tangential trial elastic stress rates. This mis-partitioning of the relative magnitudes of elastic and plastic strain rates can lead to a misassessment of the extent of non-normality in a problem.

- *Miscalculation of the yield surface normal.* Phantom non-normality will result if the flow direction \mathbf{M} is compared against an improperly evaluated yield surface normal \mathbf{N} . This can happen when using an inadmissible yield function that violates the requirement that $f > 0$ for all points outside the yield surface. For example, a remarkably persistent myth [47, 82] in plasticity literature claims that the Tresca yield function can be expressed as a polynomial expansion, $f = 4J_2^3 - 27J_3^2 - 36\tau_y^2 J_2^2 + 96\tau_y^4 J_2 - 64\tau_y^6$, where τ_y is the yield stress in shear. However, regions *outside* the correct Tresca yield surface exist for which this deficient yield function is negative, which is unacceptable.
- *Mistaking pressure-sensitivity for hardening (or vice versa).* Figure 6.9 showed that pressure sensitivity affects nonhardening stress–strain plots. Figure 6.10 shows meridional stress trajectories for these problems, as well as *difference* (axial minus lateral) stress–strain plots. If a von Mises material hardens linearly, the stress difference increases linearly while \mathbf{M} remains purely deviatoric, but the same loading response can be due to pressure sensitivity in a nonhardening model for which \mathbf{M} is not deviatoric. Thus, different interpretations of a stress–strain plot can lead to conflicting assessments of the flow direction.
- *Inappropriateness of local theories?* Bažant [3] has argued that nonlocal theory can account for observed material response that would otherwise appear to be nonnormality in simpler local plasticity models. An appropriate avenue for continued research would be to demonstrate that a nonlocal theory like Bažant’s is incapable of the spontaneous motion from a quiescent state that is possible with nonassociative local theories (see p. 251).

To conclude, the question of whether or not nonassociative plastic response is real—or simply an artifact of misinterpreted data (or data interpreted in the context of an overly simplistic model)—remains debatable. Arguments favoring nonassociativity must be bolstered include assurances that the above-listed mis-assessments of the flow direction (or violations of fundamental tenets of thermodynamics) have been ruled out. Although purely micromechanical models [2, 34, 37, 59] often fall short of quantitative predictions, this category of research seems most promising for explaining the *trends* in data that are modeled in phenomenological models as nonassociativity *without constraints on the domain of applicability*.

Incidentally, as discussed on p. 268, if nonassociativity actually exists, then an otherwise linearly elastic material will admit plastic waves that overdrive elastic waves (i.e., no elastic precursor), which is a phenomenon traditionally (and probably better) explained by nonlinearity of the elastic response rather than nonassociativity.

6.6 Rate Dependence

This section addresses rate dependence, where it is argued that plastic shock waves probably do not exist, but are instead diffusive (they cannot form as a nearly jump discontinuity). It can be shown [6] that attempting to use rate-independent plasticity to model a plastic-plastic wave (i.e., a sharp transition from one state at yield to another) results in a violation of the principle of maximum plastic work. When including rate dependence, plastic waves diffuse spatially and temporally because steady-state plastic flow requires finite time to develop.

As sketched in Fig. 6.11, the hallmark of a rate-dependent material is an *apparent* increase in strength with increasing strain rate. Early efforts to model rate dependence simply allowed the material strength to be a function of strain rate; more generally, the yield function was allowed to depend on strain rate (see, e.g. [66] or [17]). While this strategy can give satisfactory predictions for monotonic proportional loading, it can lead to paradoxical results that are inconsistent with observations of unloading and transient strain rates (e.g., wave interactions). If, for example, a large strain is applied suddenly and then (as in shock loading) held constant, one would expect a large initial stress that decays over time (microseconds) down to the quasistatic yield stress. However, if a model takes yield stress to be a function of strain rate, this drop in stress will be *instantaneous*, which is not desired.

At the heart of many rate-dependent models is the notion that a material's *elastic* response is nearly instantaneous, while inelastic response is comparatively "sluggish" (viscous). Viscoplastic models typically presume that *the inelastic strain rate is independent of the total strain rate*. Instead, the inelastic strain rate depends only on state variables, possibly including internal state variables whose values are assigned with knowledge of the history of the deformation. In this section, we will present a generalized Duvaut-Lions

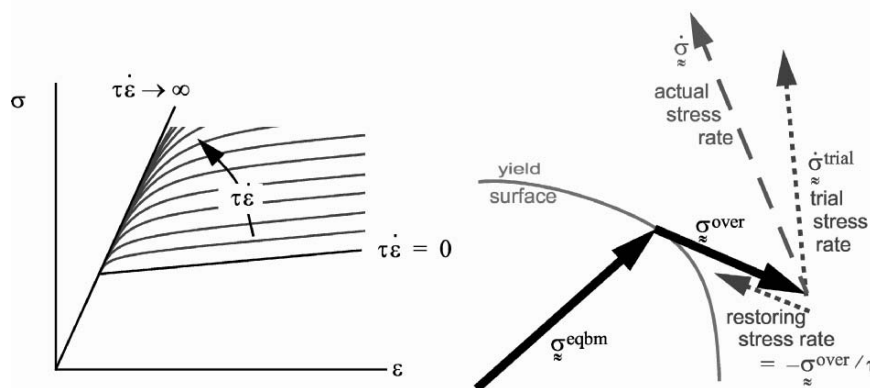


Fig. 6.11. Overstress rate dependence

“overstress” model [18] (based on the pioneering work of Perzyna [68]) in which the inelastic strain rate is presumed to depend only on the distance between the stress $\boldsymbol{\sigma}$ (which can lie transiently off the yield surface) and the quasistatic stress $\boldsymbol{\sigma}^{\text{eqbm}}$ (which is constrained to lie always on or within the yield surface, and which is updated through time using the rate-independent plasticity equations that were presented earlier in this chapter). The strain rate is decomposed as the sum of an elastic part $\dot{\boldsymbol{\epsilon}}^e$ plus a *viscoplastic* part $\dot{\boldsymbol{\epsilon}}^{\text{VP}}$:

$$\dot{\boldsymbol{\epsilon}} = \dot{\boldsymbol{\epsilon}}^e + \dot{\boldsymbol{\epsilon}}^{\text{VP}}. \quad (6.74)$$

The viscoplastic strain rate $\dot{\boldsymbol{\epsilon}}^{\text{VP}}$ depends only on the instantaneous material state, not on the total strain rate or any other rates of change in the state. Specifically, the viscoplastic strain rate is governed by

$$\dot{\boldsymbol{\epsilon}}^{\text{VP}} = \frac{1}{\tau} \mathbb{E}^{-1} : \boldsymbol{\sigma}^{\text{over}}, \quad \text{where } \boldsymbol{\sigma}^{\text{over}} = \boldsymbol{\sigma} - \boldsymbol{\sigma}^{\text{eqbm}}. \quad (6.75)$$

The fourth-order tensor \mathbb{E}^{-1} is the elastic compliance (inverse of the stiffness), τ is a material parameter called the relaxation time, and $\boldsymbol{\sigma}^{\text{eqbm}}$ is the rate-independent stress solution that is governed by the rate-independent plasticity equations. Loosely speaking, $\boldsymbol{\sigma}^{\text{over}}$ is the amount by which the dynamic yield stress exceeds the quasistatic yield stress.

Because (6.75) states that the stress $\boldsymbol{\sigma}$ is the sum of the quasistatic “equilibrium” stress $\boldsymbol{\sigma}^{\text{eqbm}}$ plus the overstress $\boldsymbol{\sigma}^{\text{over}}$ (both of which are illustrated in Fig. 6.11), computing the time history of stress requires evolution equations for the equilibrium stress and the overstress. The equilibrium stress evolves through time via the rate-independent plasticity equations described earlier, so its value may be tracked through time via standard rate-independent plasticity. We now present the incremental equations governing evolution of the overstress $\boldsymbol{\sigma}^{\text{over}}$.

Neglecting elastic–plastic coupling, the stress rate is, as usual, given by the elastic stiffness acting on the elastic part of the strain rate: $\dot{\sigma}_{ij} = E_{ijkl} \dot{\epsilon}_{kl}^e$. Applying the stiffness to both sides of (6.74) and using (6.75) allows the stress rate to be written

$$\dot{\boldsymbol{\sigma}} = \dot{\boldsymbol{\sigma}}^{\text{trial}} - \frac{1}{\tau} \boldsymbol{\sigma}^{\text{over}}, \quad (6.76)$$

where, as usual, $\dot{\sigma}_{ij}^{\text{trial}} \equiv E_{ijkl} \dot{\epsilon}_{kl}$. Equation (6.76) states that the actual stress rate (long-dashed line in Fig. 6.11) is the sum of the two limiting stress rates that are depicted as short-dashed lines in Fig. 6.11. The restoring stress rate is continually attracted toward the equilibrium stress, and will reach it eventually unless an applied strain rate generates a counteracting trial stress rate.

Subtracting $\dot{\boldsymbol{\sigma}}^{\text{eqbm}}$ from both sides of (6.76) gives the evolution law governing the overstress:

$$\boxed{\dot{\boldsymbol{\sigma}}^{\text{over}} = \dot{\boldsymbol{\sigma}} - \frac{\boldsymbol{\sigma}^{\text{over}}}{\tau}} \quad \text{where } \dot{\boldsymbol{\sigma}} \equiv \dot{\boldsymbol{\sigma}}^{\text{trial}} - \dot{\boldsymbol{\sigma}}^{\text{eqbm}}. \quad (6.77)$$

This set of linear first-order differential equations may be integrated exactly *provided that $\dot{\boldsymbol{\sigma}}$ is known as a function of time throughout the time interval of interest.*

Analytical Solutions

The tensor $\dot{\mathbf{a}}$ is the amount by which the elastic trial stress rate exceeds the equilibrium stress rate. In many problems of practical interest, both the trial and the equilibrium stress rates are constant over a significant time interval. In this case when τ and $\dot{\mathbf{a}}$ are constant over a finite time interval from t_0 to t , the exact solution to the ordinary first-order differential equation in (6.77) is

$$\sigma^{\text{over}}(t) = \tau \dot{\mathbf{a}} [1 - e^{-(t-t_0)/\tau}] + \sigma^{\text{over}}(t_0) [e^{-(t-t_0)/\tau}]. \quad (6.78)$$

As a special case, suppose that $t_0 = t^{\text{yield}}$, where t^{yield} is the time at which the yield surface is first reached following elastic loading. Then the overstress is zero at $t_0 = t^{\text{yield}}$, and the above solution specializes to

$$\sigma^{\text{over}}(t) = \begin{cases} \mathbf{0} & \text{for } t > t^{\text{yield}} \\ \tau \dot{\mathbf{a}} [1 - e^{-(t-t^{\text{yield}})/\tau}] & \text{for } t < t^{\text{yield}} \end{cases}. \quad (6.79)$$

Importantly, (6.78) must apply during *both* plastic loading and elastic unloading. During elastic unloading, the trial and equilibrium stress *rates* are equal, so that $\dot{\mathbf{a}} = \mathbf{0}$. However, the trial and equilibrium stress *states* are generally not equal. In other words, σ^{over} does not drop instantaneously to zero upon unloading; instead, it *decays toward zero*. In this case where $\dot{\mathbf{a}} = \mathbf{0}$ but $\sigma^{\text{over}} \neq \mathbf{0}$, (6.78) specializes to

$$\sigma^{\text{over}}(t) = [\sigma^{\text{over}}(t_0) e^{-(t-t_0)/\tau}] \quad (6.80)$$

When unloading, the overstress decreases exponentially in magnitude, allowing the dynamic stress to “catch up” with the quasistatic stress. Equation (6.78) is very general because it applies to *any choice for the quasistatic (inviscid) yield model that governs the quasistatic stress* σ^{eqbm} , including hardening and softening models. Equations (6.79) and (6.80) are merely specializations for two classes of applied strain rates (monotonic loading and unloading). Even for monotonic loading, however, strain rate influences material response, as illustrated in Fig. 6.12.

We will now discuss further specializations of these general results to better illustrate their meaning and to progress toward statements of simple analytical problems that may be used to verify numerical implementations of overstress theory. Recalling that $\dot{\sigma}^{\text{eqbm}}$ satisfies the inviscid plasticity equations, note that

$$\dot{\mathbf{a}} = \mathbb{E} : \dot{\epsilon}^{\text{P}}, \quad (6.81)$$

where $\dot{\epsilon}^{\text{P}}$ is the plastic strain rate from the *inviscid* problem. In other words, $\dot{\mathbf{a}}$ is simply the last term in (6.33):

$$\dot{\mathbf{a}} = \frac{\mathbf{P} (\mathbf{N} : \dot{\sigma}^{\text{trial}})}{\mathbf{P} : \mathbf{N} + H}. \quad (6.82)$$

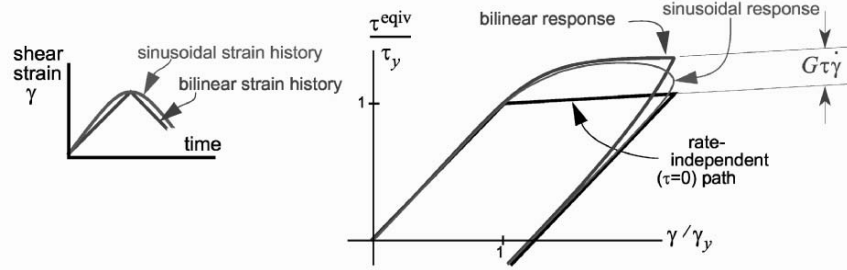


Fig. 6.12. Overstress rate dependence. When loaded through identical pure shear strain values at different rates, the bilinear response approaches an *apparent* steady-state strength, but the sinusoidal response remains transient

For classical von Mises plasticity, this specializes to

$$\dot{\mathbf{a}} = 2G\hat{\mathbf{S}}(\hat{\mathbf{S}} : \dot{\boldsymbol{\epsilon}}^d), \quad (6.83)$$

where G is the shear modulus, $\hat{\mathbf{S}}$ is a unit tensor in the direction of the stress deviator, and $\dot{\boldsymbol{\epsilon}}^d$ is the deviatoric part of the total strain rate. For monotonic proportional loading at a constant strain rate, the stress deviator will be parallel to the strain rate deviator, so that (6.83) simplifies to $\dot{\mathbf{a}} = 2G\dot{\boldsymbol{\epsilon}}^d$, and (6.79) specializes (*for von Mises models only*) to

$$\boldsymbol{\sigma}^{\text{over}}(t) = \begin{cases} \mathbf{0} & \text{for } t > t^{\text{yield}} \\ 2G\tau\dot{\boldsymbol{\epsilon}}^d [1 - e^{-(t-t^{\text{yield}})/\tau}] & \text{for } t < t^{\text{yield}} \end{cases} \quad (6.84)$$

For example, if the strain rate is a pure shear, then after the onset of yield,

$$\sigma_{12}^{\text{over}} = \sigma_{12} - \sigma_{12}^{\text{eqbm}} = 2G\tau\dot{\epsilon}_{12} [1 - e^{-(t-t^{\text{yield}})/\tau}]. \quad (6.85)$$

For uniaxial strain (common in shock-physics), only the axial component of strain ϵ_{11} varies, while all other strains are zero. In this case, the axial component of the strain *deviator* is $2\epsilon_{11}/3$ while the lateral component is $-\epsilon_{11}/3$. Therefore

$$\sigma_{11}^{\text{over}} = \sigma_{11} - \sigma_{11}^{\text{eqbm}} = \frac{4G}{3}\tau\dot{\epsilon}_{11} [1 - e^{-(t-t^{\text{yield}})/\tau}], \quad (6.86)$$

$$\sigma_{22}^{\text{over}} = \sigma_{22} - \sigma_{22}^{\text{eqbm}} = \frac{-G}{3}\tau\dot{\epsilon}_{11} [1 - e^{-(t-t^{\text{yield}})/\tau}]. \quad (6.87)$$

The apparent axial strength increases, but the lateral stress *decreases*. These solutions demonstrate that the amount by which the dynamic strength exceeds the quasistatic strength (under monotonic proportional loading of a von Mises material) approaches a constant steady state value that varies linearly with the strain rate if the characteristic response time τ is constant. A computational

example for uniaxial strain loading is presented on p. 259. Experimental data for geological materials suggest that the value of τ varies according to the underlying microphysical processes (specifically, the response time for pore collapse is different from that for microcrack growth [23]). A dramatic change in strain rate sensitivity (i.e., a change in the value of τ) has also been noted for copper ([69], where the rate effects are very accurately modeled using fundamental materials science principles rather than the phenomenological approach described here). In general, τ is usually treated as a material state function, not a constant.

Numerical Solutions

In numerical plasticity models, the total strain rate is treated as if it were constant over the time step, in which case, the trial and equilibrium stress rates—and therefore $\dot{\mathbf{a}}$ —are regarded as approximately constant. Consequently, the analytical solution in (6.78) may be applied during the time step to obtain an optimally accurate stress update. For a numerical time step, from $t = t_n$ to $t = t_{n+1}$, (6.78) may be written

$$\boldsymbol{\sigma}_{n+1}^{\text{over}} = \tau \dot{\mathbf{a}} [1 - e^{-(t_{n+1}-t_n)/\tau}] + \boldsymbol{\sigma}_n^{\text{over}} [e^{-(t_{n+1}-t_n)/\tau}] \quad (6.88)$$

or

$$\boldsymbol{\sigma}_{n+1}^{\text{over}} = \dot{\mathbf{a}} \Delta t \left[\frac{1 - e^{-\Delta t/\tau}}{\Delta t/\tau} \right] + \boldsymbol{\sigma}_n^{\text{over}} [e^{-\Delta t/\tau}] \quad (6.89)$$

When the total strain rate $\dot{\boldsymbol{\epsilon}}$ is constant, $\dot{\boldsymbol{\sigma}}^{\text{trial}}$ will be constant. However, for time steps that are only partly plastic, $\dot{\boldsymbol{\sigma}}^{\text{eqbm}}$ will not be constant even if the strain rate $\dot{\boldsymbol{\epsilon}}$ is constant. To minimize the error associated with using an analytical solution that presumes $\dot{\mathbf{a}}$ is constant, recall that $\dot{\mathbf{a}} \equiv \dot{\boldsymbol{\sigma}}^{\text{trial}} - \dot{\boldsymbol{\sigma}}^{\text{eqbm}}$ so that $\dot{\mathbf{a}} \Delta t$ is best approximated in numerical settings by the *increment*

$$\dot{\mathbf{a}} \Delta t = (\boldsymbol{\sigma}_{n+1}^{\text{trial}} - \boldsymbol{\sigma}_n^{\text{trial}}) - (\boldsymbol{\sigma}_{n+1}^{\text{eqbm}} - \boldsymbol{\sigma}_n^{\text{eqbm}}), \quad (6.90)$$

where

$$\boldsymbol{\sigma}_n^{\text{trial}} = \boldsymbol{\sigma}_n \quad \text{and} \quad \boldsymbol{\sigma}_{n+1}^{\text{trial}} = \boldsymbol{\sigma}_n + \mathbb{E} : \dot{\boldsymbol{\epsilon}} \Delta t. \quad (6.91)$$

The equilibrium stress must be available at both the beginning and the end of the step, which requires it to be saved as an internal state variable. Its value at the beginning of the step, $\boldsymbol{\sigma}_n^{\text{eqbm}}$, can be retrieved from the state variable array, and its value at the end of the step, $\boldsymbol{\sigma}_{n+1}^{\text{eqbm}}$, is computed by integrating the rate-independent (inviscid) plasticity equations discussed earlier in this chapter. Substituting (6.90) into (6.89), the overstress is therefore updated during a numerical time step according to

$$\boldsymbol{\sigma}_{n+1}^{\text{over}} = [(\boldsymbol{\sigma}_{n+1}^{\text{trial}} - \boldsymbol{\sigma}_n) - (\boldsymbol{\sigma}_{n+1}^{\text{eqbm}} - \boldsymbol{\sigma}_n^{\text{eqbm}})] R_H + \boldsymbol{\sigma}_n^{\text{over}} [R_H - r_h], \quad (6.92)$$

where

$$R_H = \frac{1 - e^{-\Delta t/\tau}}{\Delta t/\tau} \quad \text{and} \quad r_h = R_H - e^{-\Delta t/\tau}. \quad (6.93)$$

Alternative viscoplastic integration schemes that are unified with the quasi-static integration are reviewed by De Borst and Heeres [13].

Incidentally, overstress models typically also monitor equilibrium and dynamic values of ISVs. Each ISV η_k is typically evolved according to

$$\dot{\eta}_k = \frac{-1}{\tau} [\eta_k - \eta_k^{\text{eqbm}}]. \quad (6.94)$$

Using methods similar to what was done for stress, the ISV numerical update is similar to (6.92) but with $r_h = 0$ (ISVs always respond “sluggishly”; r_h is nonzero only for variables, like stress, that can change nearly instantaneously during elastic loading).

Example: Uniaxial Strain of a Von Mises Material

In this section, we illustrate some basic features of rate dependence for a contrived nonhardening von Mises material subjected to homogenous uniaxial strain loading. Among the material parameters quoted in Table 6.1, those listed under the thick line are derived from the minimal input parameters above the line.

This material was analyzed using a computational material model that updates stress using the Duvaut–Lions overstress theory described in the previous section. The *total* uniaxial strain history $\epsilon(t)$ in the top row of Fig. 6.13 was the input forcing function, whereas the elastic and plastic strain histories, $\epsilon^e(t)$ and $\epsilon^p(t)$, are among the outputs. Identical total strain values were applied in both problems, but at a rate $100\times$ faster in the high rate example. Given sufficient time to reach steady state, the *slopes* of the elastic and plastic strain histories approach the same values for both slow and fast loading even though the *values* differ. Likewise, the stress–strain response asymptotes to

Table 6.1. Parameters used in rate-dependence demo

Density ρ	7849 kg m ⁻³
Yield in uniaxial stress Y	285.788
Bulk modulus K	142 GPa
Shear modulus G	79 GPa
Characteristic response time τ	10^{-5} s
<hr/>	
Constrained elastic modulus, $C = K + 4G/3$	247 GPa
Elastic wave speed, $c_L = \sqrt{C/\rho}$	5.6 km s ⁻¹
Yield in shear, $\tau^{\text{yield}} = Y/\sqrt{2}$	165 MPa
Hugoniot elastic limit, $\sigma^{\text{yield}} = \sigma^{\text{HEL}} = Y \frac{1-\nu}{1-2\nu}$	448 MPa
Uniaxial strain at HEL yield, $\epsilon^{\text{yield}} = \sigma^{\text{HEL}}/C$	0.0018

the same slope for both high and low rates, which gives a higher apparent yield stress for the high-rate problem. This example used a nonhardening material specifically to demonstrate that the curved transient part of the stress–strain response is *not* necessarily the result of hardening, as is often asserted [68]. Multiple experiments at different loading rates (preferably with unloading) are necessary to determine if the so-called “hardening” part of the plastic wave is attributable to hardening, rate effects, or pressure dependence [93]. When hardening and rate dependence are both included in a plasticity model, as in Fig. 6.12, the hardening primarily influences the equilibrium response curve upon which the overstress is superimposed.

Note that the overstress in Fig. 6.13 approaches steady state under monotonic loading in a time interval of about 5τ . Thus, if measured time-resolved stress histories are available, “time-to-steady-state” can be a good indicator of a material’s characteristic relaxation time τ . Specifically, if T denotes the time required for the overstress to reach half of its steady-state value, then $\tau \approx T / (\ln 2)$. Alternatively, if stress–strain data are available at both high and low rates, then the material response time may be computed from the slope of a plot of apparent steady state HEL strength vs. strain rate:

$$\tau = \frac{\sigma_{\text{steady-state}}^{\text{over}}}{\frac{4}{3}G\dot{\epsilon}}. \quad (6.95)$$

This rule of thumb has been here derived based on an assumption that the underlying yield threshold is pressure-independent von Mises and the loading is uniaxial strain. For other types of loading or when the yield stress is pressure dependent, this rule no longer applies.

Equation (6.95) implies that dynamic strength varies linearly with strain rate, which is at odds with numerous observations ([93], where strength varies with strain rate according to a power law). Also, strain-rate dependence is known to vary with temperature [49], which (for the adiabatic conditions applicable in shock physics problems) implies a dependence on entropy and therefore on the accumulated plastic work. Consequently, implementations of Duvaut–Lions rate dependence models might allow the characteristic response time τ to vary with plastic strain [22] and/or the magnitude of the overstress.

Rate dependence naturally plays a crucial role in shock loading, where strain changes are applied *very rapidly* over a short interval. “Sluggishness” of viscoplastic response in Fig. 6.13 prevents slope discontinuities in high-rate loading except where the strain history itself has a slope discontinuity. During shock (or very rapid) loading, the first term in (6.78) predominates because $\dot{\mathbf{a}}$ is significantly different from zero. Consequently, shock loading quickly produces a large overstress, leaving the material in an excited “overplastic” state. Once a shock has passed, however, the strain rate becomes considerably smaller, making $\dot{\mathbf{a}}$ quite small, therefore allowing the *last* term in (6.78) to predominate postshock material response wherein the overstress decays to zero, allowing the shocked state to approach the equilibrium plastic state.

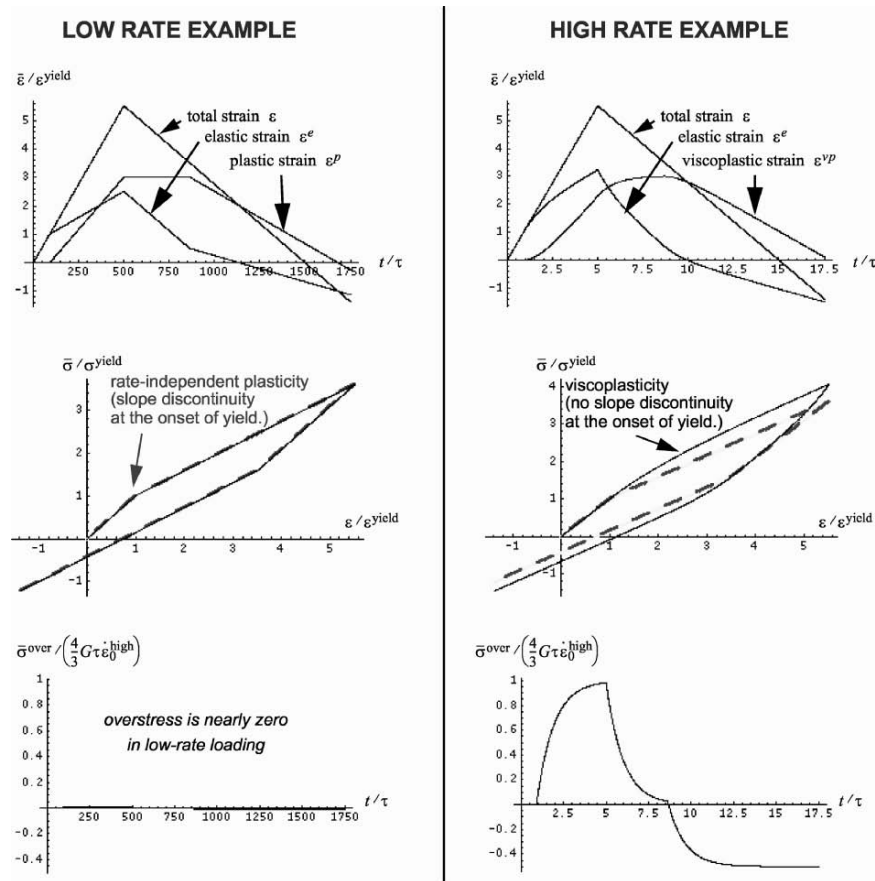


Fig. 6.13. The effect of strain rate in uniaxial strain. The axes normalizations are defined in Table 6.1. All stresses and strains are the axial component. The dashed lines show the quasistatic (inviscid) solution

Figure 6.13 illustrates how a stress–strain plot is affected by strain rate. The speed at which a uniaxial strain signal propagates is given by $\sqrt{s/p}$, where s is the slope of the stress vs. strain plot. In Fig. 6.13, the tangent modulus “ s ” is constant during the initial elastic loading but drops *continuously* after the onset of yield during high rate loading. Thus, the stress pulse “splits” into a fast-moving elastic precursor followed by a *continuously slower* plastic signal. This is only *one* possible reason why the plastic wave shown in Fig. 6.14 develops without a jump discontinuity. However, comparing Figs. 6.13, 6.10, and 6.5 a curved postyield stress–strain response (leading to a structured diffusive-like plastic wave) can also result from *rate-independent* hardening or pressure-dependence of strength. A single plate-impact experiment cannot determine conclusively which phenomenon is occurring—multiple experiments,

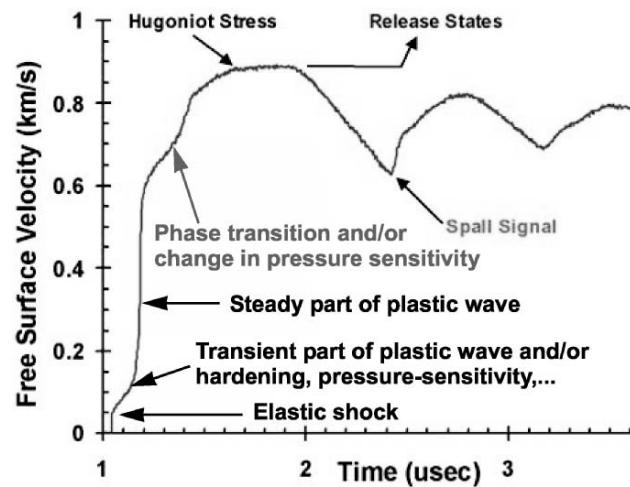


Fig. 6.14. A prototypical VISAR record

preferably with re-shock and release, are required. Similarly, the third signal in Fig. 6.14 is typically interpreted as a phase transition (which is likely for that particular material, AERMET steel), but signals like it can also occur without a phase transition if the yield surface transitions rapidly from a cone to a cylinder, as often assumed for brittle materials [36].

Because the speed of the plastic signal drops continuously, a *plastic shock* (i.e., an arbitrarily rapid change in the plastic strain) is impossible. Instead, under viscoplasticity theory, the rate at which plastic strain can accumulate is limited by the material's characteristic response time. Moreover, when the slope s of the stress-strain curve is negative, as during material softening or relaxation from an over-plastic state, the process becomes diffusive, once again disallowing shocks. Gilman and others [24,25,33] have long argued that, because plastic deformation is dissipative, plastic shocks cannot exist. Instead, Gilman argues, plastic deformation must be *diffusive*. This view is substantiated here using an overstress model. A rate-independent von Mises model, on the other hand, admits a slope discontinuity at the onset of yield, making an elastic-plastic shock *mathematically* possible in this idealized case. Thus, whether or not a plastic shock can be modeled depends on whether or not the constitutive model admits instantaneous plastic response under an instantaneously applied strain increment. Whether or not a plastic shock is *admissible* (which is an entirely different question) requires thermodynamical arguments like those of Gilman (also see [83]). If such arguments disallow jumps in plastic strain, then rate-independent models must be ruled out. A related question is whether a plastic-plastic shock (i.e., one for which the material is at yield both ahead of and behind the shock) is possible under overstress theory. This question leads us to consider reloading scenarios.

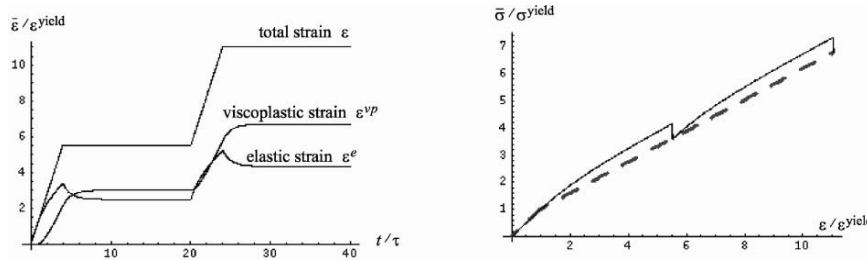


Fig. 6.15. Rate dependence produces sudden changes in the stress–strain tangent modulus upon reshock

Consider a strain that is applied suddenly and held constant, followed later by a second (similarly applied) increase in strain. An overstress model predicts the material response shown in Fig.6.15. During the period when the strain is first held constant, an overstress model allows the stress (and therefore the elastic strain) to decay *continuously over time (microseconds)* to its equilibrium value (the drop is a step discontinuity in a stress–strain plot because strain is held constant).

Upon application of the second suddenly applied strain, the tangent modulus s again equals the *elastic* tangent modulus despite the fact that the material remains at yield. Thus, overstress models predict that the re-loading wave will propagate as a smooth (diffuse) plastic signal just like the first wave, having a smoothly developing stress increase *without a significant elastic precursor*. Thus, overstress theory does not admit a plastic–plastic shock discontinuity (a more sophisticated model would be required if an elastic precursor is evident in reshock data). For a rate-independent idealization, it has been proved [6] that a plastic–plastic shock violates the maximum plastic work inequality even when advanced constitutive features such as pressure-dependence and nonnormality are included. Thus, plastic–plastic shocks are thermodynamically inadmissible for rate-independent plasticity. Conclusions like these are typically derived under the assumption that elastic stiffnesses are constant, which is not realistic and hence warrants generalizing the analyses to include nonlinear elasticity.

6.7 Plastic Wave Speeds

The previous section argued that plastic shocks (jump discontinuities in plastic strain) probably do not exist. Shock loading produces a split wave form consisting of an elastic precursor followed by a continuous plastic “wave,” as illustrated in Fig.6.14. This section hypothesizes that the apparent plastic wave seen in velocity interferometry data corresponds to the point at which plastic flow has reached a steady state so that the slope of the dynamic stress–strain plot is identical to the slope of the rate-independent plot. As such, the

propagation speed (i.e., the time derivative of position holding the *peak* stress constant) can be determined from the eigenvalues of the acoustic tensor associated with the *rate-independent* plastic tangent modulus.

For acceleration waves that are rapid rather than mathematically discontinuous, the well-known Rankine–Hugoniot jump conditions (that follow from conservation of mass and momentum) along with a compatibility constraint (that follows from demanding continuous displacements) imply the incremental condition [9, 31],

$$d\boldsymbol{\varepsilon} = \frac{1}{\rho c^2} \left[\frac{\mathbf{n}(d\mathbf{t}) + (d\mathbf{t})\mathbf{n}}{2} \right], \quad \text{where } d\mathbf{t} = d\boldsymbol{\sigma} \cdot \mathbf{n}. \quad (6.96)$$

Here, \mathbf{n} is the unit normal of the acceleration wave surface (multiplied dyadically by the traction increment $d\mathbf{t}$), ρ is mass density, c is the wave propagation speed, and \mathbf{t} is traction ($\mathbf{t} = \boldsymbol{\sigma} \cdot \mathbf{n}$). Incidentally, ρc^2 is actually an approximation of $(\rho c)c_0$, where c_0 is the reference configuration wave speed and c is the spatial wave speed [6]. Except across material interfaces, conservation of mass requires both c_0 and the impedance ρc to be individually continuous across the sharp transition zone. Hence ρc^2 may also be treated as constant.

Suppose that the stress and strain increments are further related by a constitutive relationship of the form

$$d\boldsymbol{\sigma} = \mathbb{T} : d\boldsymbol{\varepsilon}, \quad (6.97)$$

where the “tangent stiffness” \mathbb{T} is determined from the state of the material (possibly including history-dependent internal state variables), but is unaffected by the rate of change in the state. In other words, we are seeking the wave speeds associated with the rate-independent part of a rate-dependent viscoplastic model. Requiring (6.96) and (6.97) to *both* be true leads to the well-known acoustic eigenvalue problem,

$$\mathbf{A} \cdot \mathbf{w} = \lambda \mathbf{w}, \quad \text{where } \mathbf{w} = d\mathbf{t} \quad \text{and} \quad \lambda = \rho c^2. \quad (6.98)$$

Here, the *acoustic tensor* \mathbf{A} (unrelated to the tensor \mathbf{A} that was used previously in (6.60)) is defined

$$\mathbf{A} \equiv \mathbf{n} \cdot \mathbb{T} \cdot \mathbf{n}. \quad (A_{ij} = n_p T_{pijq} n_q). \quad (6.99)$$

Equation (6.98) expresses the well-known result that ρc^2 and $d\mathbf{t}$ must be, respectively, an eigenvalue and associated eigenvector of the plastic acoustic tensor. They cannot be selected independently.

Consider now a tangent stiffness of the form

$$\mathbb{T} = \mathbb{E} - \frac{1}{\eta} \mathbf{P} \mathbf{Q}. \quad (6.100)$$

For a plasticity model, the tensors \mathbf{P} and \mathbf{Q} and the scalar η are given in (6.36):

$$\mathbf{P} \equiv \mathbb{E} : \mathbf{M} + \mathbf{Z}, \quad \mathbf{Q} = \mathbb{E} : \mathbf{N}, \quad \text{and} \quad \eta = \mathbf{M} : \mathbb{E} : \mathbf{N} + H. \quad (6.101)$$

These expressions, which apply to plasticity theory, are not needed per se to derive the solution of the eigenproblem. That is, the eigenvalue solution presented in this section is purely mathematical, allowing \mathbf{P} , \mathbf{Q} , and η to have *any* physical meaning. We will, however, use adjectives appropriate to plasticity theory when *discussing* variables.

Dotting (6.100) from the left and right by \mathbf{n} , the plastic acoustic tensor is

$$\mathbf{A} \equiv \mathbf{A}^e - \frac{1}{\eta} \mathbf{p} \mathbf{q}, \quad \left[A_{ij} = A_{ij}^e - \frac{1}{\eta} p_i q_j \right], \quad (6.102)$$

where the elastic acoustic tensor is

$$\mathbf{A}^e \equiv \mathbf{n} \cdot \mathbb{E} \cdot \mathbf{n} \quad (6.103)$$

and

$$\mathbf{p} = \mathbf{P} \cdot \mathbf{n} \quad \text{and} \quad \mathbf{q} = \mathbf{Q} \cdot \mathbf{n}. \quad (6.104)$$

We aim to express the eigenvalues and eigenvectors of the plastic acoustic tensor \mathbf{A} in terms of the eigenvalues and eigenvectors of the elastic acoustic tensor \mathbf{A}^e . Assuming that the elastic stiffness \mathbb{E} is major symmetric and positive definite, the *elastic* acoustic tensor will be symmetric and positive definite (hence it will have positive real eigenvalues and mutually orthogonal eigenvectors). However, if $\mathbf{p} \neq \mathbf{q}$, then the *plastic* acoustic tensor is nonsymmetric, and complex eigenvalues are possible (flutter instability). Even if $\mathbf{p} = \mathbf{q}$, the fact that the dyad $\mathbf{p} \mathbf{q}$ is *subtracted* from the positive definite elastic acoustic tensor in (6.102) implies that the plastic acoustic tensor might have negative eigenvalues. Recalling that eigenvalues of the acoustic tensor equal ρc^2 , a negative eigenvalue would imply a *complex* wave speed. Regarding such an event as a bifurcation from a stable solution, the occurrence of a zero eigenvalue (which implies a stationary discontinuity) has often been used as a criterion for the onset of localization of material deformation into narrow shear bands [54, 75, 98, 99].

When the elastic stiffness \mathbb{E} is anisotropic, the elastic acoustic tensor can have three distinct real eigenvalues $\{\lambda_1^e, \lambda_2^e, \lambda_3^e\}$. Letting $\{\hat{\mathbf{w}}_1^e, \hat{\mathbf{w}}_2^e, \hat{\mathbf{w}}_3^e\}$ denote the associated *normalized* eigenvectors, it can be shown [6] that the characteristic equation for the plastic eigenvalues is

$$\begin{aligned} & (\lambda - \lambda_1^e)(\lambda - \lambda_2^e)(\lambda - \lambda_3^e) \\ & + \theta_1(\lambda - \lambda_2^e)(\lambda - \lambda_3^e) + (\lambda - \lambda_1^e)\theta_2(\lambda - \lambda_3^e) + (\lambda - \lambda_1^e)(\lambda - \lambda_2^e)\theta_3 = 0, \end{aligned} \quad (6.105)$$

where

$$\theta_k = \frac{1}{\eta} (\hat{\mathbf{w}}_k^e \cdot \mathbf{p}) (\mathbf{q} \cdot \hat{\mathbf{w}}_k^e) \quad (\text{no implied sum}). \quad (6.106)$$

Each θ_k is determined directly from the tangent stiffness tensor and the jump surface normal \mathbf{n} . Hence, for a given wave front normal \mathbf{n} , each θ_k may be regarded as known (and very easy to compute).

It might be tempting to divide both sides of (6.105) by $(\lambda - \lambda_1^e)(\lambda - \lambda_2^e)(\lambda - \lambda_3^e)$ to write it as

$$\frac{\theta_1}{(\lambda - \lambda_1^e)} + \frac{\theta_2}{(\lambda - \lambda_2^e)} + \frac{\theta_3}{(\lambda - \lambda_3^e)} = -1. \quad (6.107)$$

However, doing so presumes that no plastic eigenvalue equals an elastic eigenvalue. It can be shown [6] that the eigenvector associated with a distinct plastic eigenvalue λ that is *not equal* to an elastic eigenvalue is given by

$$\mathbf{w} = (\mathbf{A}^e - \lambda \mathbf{I})^{-1} \cdot \mathbf{p} \quad (\text{Applies only for } \lambda \neq \lambda_k^e). \quad (6.108)$$

Recall that both the elastic acoustic tensor and the vector \mathbf{p} depend on the normal of the moving discontinuity surface. Showing this dependence explicitly, (6.108) is

$$\mathbf{w} = (\mathbf{n} \cdot \mathbb{E} \cdot \mathbf{n} - \lambda \mathbf{I})^{-1} \cdot \mathbf{P} \cdot \mathbf{n} \quad (\text{Applies only for } \lambda \neq \lambda_k^e). \quad (6.109)$$

Equation (6.105), which applies for arbitrary elastic anisotropy, has been studied in various forms [94], but to illustrate some basic points we now consider isotropic linear elasticity. If the elastic tangent stiffness is isotropic with a bulk modulus K and shear modulus G , the elastic acoustic tensor is

$$\mathbf{A}^e = (K + \frac{4}{3}G) \mathbf{nn} + G(\mathbf{I} - \mathbf{nn}). \quad (6.110)$$

Letting subscripts “n” and “t” stand for “normal” and “transverse” respectively, this elastic acoustic tensor has two distinct eigenvalues:

$$\text{Single-root: } \lambda_n^e = C \quad \text{associated with } \hat{\mathbf{w}} = \mathbf{n}. \quad (6.111)$$

$$\text{Double-root: } \lambda_t^e = G \quad (6.112)$$

where $C = K + \frac{4}{3}G$ is the constrained (uniaxial strain) elastic modulus. Any vector perpendicular to \mathbf{n} (i.e., a shearing mode) is an eigenvector associated with the double root. Recalling that the eigenvectors of the acoustic tensor quantify the direction of the traction jump, the single-multiplicity solution corresponds to a uniaxial compression wave traveling at speed $c = \sqrt{C/\rho}$. The double root corresponds to a simple shear wave traveling at speed $c = \sqrt{G/\rho}$. This result shows that it is impossible to *elastically* propagate a combined pressure–shear wave—the waves will always split into distinct pressure and shear (“p and s”) waves moving at distinct speeds. To the contrary, we will show that plasticity allows formation of combined pressure + shear in a single wave front.

For elastic isotropy, (6.105) simplifies to

$$[(\lambda - \lambda_n^e)(\lambda - \lambda_t^e) + \theta_n(\lambda - \lambda_t^e) + (\lambda - \lambda_n^e)\theta_t](\lambda - \lambda_t^e) = 0, \quad (6.113)$$

where

$$\theta_n = \frac{1}{\eta} (\mathbf{n} \cdot \mathbf{p}) (\mathbf{q} \cdot \mathbf{n}) \quad \text{and} \quad \theta_t = \theta_n - \frac{1}{\eta} \mathbf{p} \cdot \mathbf{q}. \quad (6.114)$$

As pointed out by Hill [32] and countless others, one solution to (6.113) is simply $\lambda = \lambda_t^e$. The nontrivial solutions depend on details of the plasticity model. Whereas elastic materials admit two wave modes (normal and shear), a plastic wave supports a broader variety of modes. These are determined by the eigenvectors of the plastic acoustic tensor \mathbf{A} . The eigenvector associated with a *nonelastic* eigenvalue λ can be computed using the general solution in (6.109). For this special case of an elastically isotropic material, that solution may be written in the form

$$\mathbf{w} = \frac{\mathbf{p}_n}{\lambda - \lambda_n^e} + \frac{\mathbf{p}_t}{\lambda - \lambda_t^e} \quad (\text{Applies only for } \lambda \neq \lambda_k^e), \quad (6.115)$$

where \mathbf{p}_n is the part of the \mathbf{p} vector in the wave propagation direction [i.e., $\mathbf{p}_n = (\mathbf{p} \cdot \mathbf{n})\mathbf{n}$] and \mathbf{p}_t is the part of \mathbf{p} tangential to the wave front. This solution shows that, in general, a plastic wave mode can include *both* normal and shear tractions (rather than one or the other, as for elastic waves in an isotropic material). For plastic eigenvalues that equal elastic eigenvalues, the wave modes are given by different solutions depending on the normal and tangential components of \mathbf{p} and \mathbf{q} , and also depending on the multiplicity of the eigenvalue (see, e.g., the equation labeled “6.46” in [6]).

With knowledge of the material state and the orientation of the shock surface, values can be computed for θ_t and θ_n . Then (6.113) gives the λ eigenvalues, from which the plastic wave propagation speed is computed by $c = \sqrt{\lambda/\rho}$. Now consider the reverse problem. Suppose you seek conditions on θ_t and θ_n that give a specified wave eigenvalue. If the eigenvalue λ is specified (or inferred from interferometry data [26]), then neither θ_t nor θ_n may be determined individually, but (6.113) is a constraint that must be satisfied by them. Specifically, θ_t and θ_n fall somewhere on a straight line defined by (6.113). If for example, one seeks conditions that favor localization ($\lambda = 0$), then (6.113) shows that a (θ_t, θ_n) pair must satisfy

$$\frac{\theta_n}{\lambda_n^e} + \frac{\theta_t}{\lambda_t^e} = 1 \quad (\text{localization condition}). \quad (6.116)$$

This general condition readily reduces to various localization criteria derived historically [77] for specialized material assumptions.

Because plastic wave modes depend on whether or not the plastic eigenvalue equals an elastic eigenvalue, it is worthwhile investigating the ordering of plastic eigenvalues relative to elastic eigenvalues. Is it possible for a plastic wave to move faster than an elastic wave? The answer is “no” for associative plasticity, but “yes” (in principle) for nonassociative plasticity. Figure 6.16 shows a family of straight lines in the space of all possible (θ_t, θ_n) pairs. Each

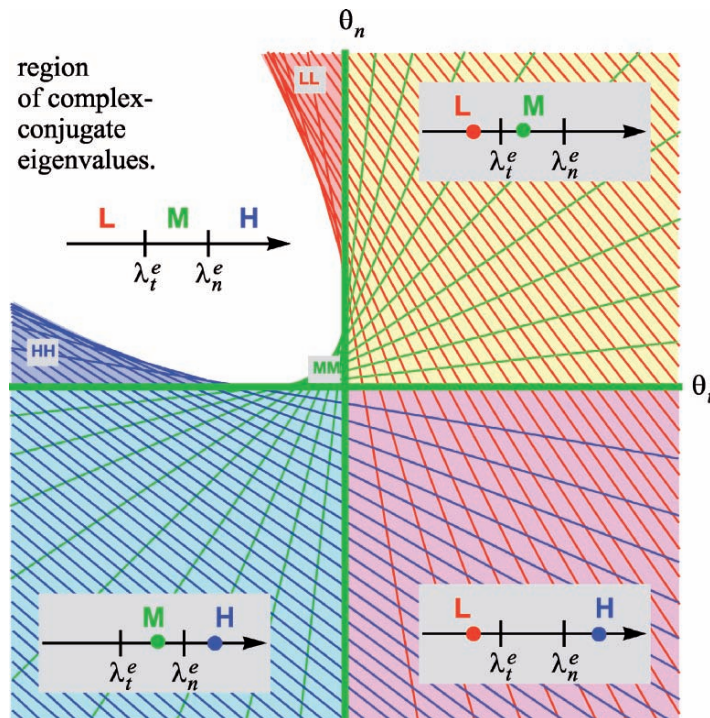


Fig. 6.16. Plastic wave eigenvalue ordering. Red, green, and blue lines (as well as labels L , M , and H) stand for the low, middle, and high portions of the number line that is split into three parts by the elastic eigenvalues. Associative (more correctly, self-adjoint) plasticity always generates points in the first quadrant, which (because it is cross-hatched by red and green lines) implies that eigenvalue ordering for self-adjoint plasticity is always of class LM (i.e., $\lambda_1 \leq \lambda_t^e \leq \lambda_2 \leq \lambda_n^e$)

straight line corresponds to a particular wave eigenvalue. The red lines show the family of (θ_t, θ_n) pairs that support a plastic eigenvalue lower than λ_t^e (i.e., slower than elastic shear waves). The blue lines show (θ_t, θ_n) pairs that support a plastic eigenvalue larger than λ_n^e , which would indicate a plastic wave that propagates *faster* than the fastest elastic speed. The green lines indicate intermediate plastic wave speeds. It can be shown [6] that associative plasticity models will always give rise to (θ_t, θ_n) pairs in the first quadrant. Hence, because this quadrant is intersected by only green and red lines, the two non-trivial plastic eigenvalues (λ_1, λ_2) will satisfy $\lambda_1 \leq \lambda_t^e \leq \lambda_2 \leq \lambda_n^e$, which is a long-established result [53] for associative plasticity. It can be shown, however, that the first and fourth quadrants in Fig. 6.16 correspond to deviatoric associativity (where, as often assumed in geomechanics, the *deviatoric parts* of the yield normal and flow direction are aligned, but their traces are different).

Hence, because the fourth quadrant is intersected by blue lines, these models can predict plastic waves that move faster than elastic waves, which is a phenomenon ordinarily (and probably more correctly) ascribed to elastic stiffening, which has been neglected here. It has been argued that an overdriven plastic shock can also develop by including thermal conductivity in the solution of the field equations [101] (something that most shock-physics codes do not support). This result, however, indicates that an alternative modeling strategy might employ *adiabatic* (no heat conduction) thermoelastic-plastic coupling of the type in (6.56) to produce phantom nonassociativity that will generate points in the fourth quadrant of Fig. 6.16.

6.8 Conclusions

This chapter has reviewed phenomenological plasticity theory with considerable emphasis on geometrical interpretations of the governing equations and computational solution methods. Discussion has focused on issues of importance for implementing *consistent* numerical constitutive plasticity models within a typical shock-physics finite element code. For example, the *unique* return direction that must be used to ensure at least first-order accuracy in elastic-predictor/plastic-corrector algorithms was shown to be aligned with *neither* the yield normal *nor* the plastic flow direction, in general. Thermodynamic and algorithmic admissibility of nonassociated yield models was debated, where several known instances of misassessed plastic flow directions were offered as possible explanations for *phantom* plastic non-normality.

Application of plasticity theory to shock physics problems here aimed to emphasize that results for von Mises theory (such as plastic incompressibility, separation of load/unload curves and even the notion that a yielded material “flows” like a fluid) do not typically hold for more realistic plasticity models, and should therefore be avoided when inferring strength from direct measurements (such as velocity interferometry data).

A typical model for viscoplastic rate-dependence was reviewed, where plastic waves were argued to be *diffusive* except possibly for pressure-dependent models with phantom non-normality where the plastic tangent stiffness tensor becomes nonmajor-symmetric and therefore admits plastic waves that travel faster than (overdrive) elastic precursor waves even without elastic stiffening.

Acknowledgment

This work was performed at Sandia National Laboratories. Sandia is a multiprogram laboratory operated by Sandia Corporation, a Lockheed Martin Company, for the United States Department of Energy under Contract DE-ALO4-04AL8500.

Frequently used symbols (others defined in context)

A	Return direction tensor without elastic–plastic coupling	$A_{ij} = E_{ijkl}M_{kl}$
E	Fourth-order elastic stiffness	$E_{ijkl} = \partial\sigma_{ij}/\partial\varepsilon_{kl}$
f	Yield function, $f(\boldsymbol{\sigma}, \eta_1, \eta_2, \dots) < 0$ if elastic	
G	Tangent elastic shear modulus	
I_1	First mechanics invariant	$I_1 = \text{tr}(\boldsymbol{\sigma})$
J_2	Second mechanics invariant	$J_2 = \frac{1}{2}\text{tr}(\mathbf{S}^2) = -\text{tr}(\mathbf{S}^C)$
J_3	Third mechanics invariant	$J_3 = \frac{1}{3}\text{tr}(\mathbf{S}^3) = \det(\mathbf{S})$
K	Tangent elastic bulk modulus	
M	Plastic flow direction (unit tensor)	
N	Unit normal to the yield surface	$\mathbf{N} = \frac{\partial f/\partial\boldsymbol{\sigma}}{\ \partial f/\partial\boldsymbol{\sigma}\ }$
P	Return direction tensor with elastic–plastic coupling	$P_{ij} = E_{ijkl}M_{kl} + Z_{ij}$
Q	Stiffness transformation of yield normal	$Q_{ij} = E_{ijkl}N_{kl}$
\bar{p}	Pressure (negative of mean stress p)	$\bar{p} = -\frac{1}{3}\sigma_{kk} = -p$
S	Deviatoric part of $\boldsymbol{\sigma}$	$S_{ij} = \sigma_{ij} - p\delta_{ij}$
T	Deviatoric part of \mathbf{S}^2	$T_{ij} = S_{ik}S_{kj} - \frac{2}{3}J_2\delta_{ij}$
δ_{ij}	Kronecker delta	$= 1$ if $i = j$, $= 0$ otherwise.
$\dot{\boldsymbol{\varepsilon}}^P$	Plastic strain rate tensor (components $\dot{\varepsilon}_{ij}^P$)	
ε^P	Equivalent total plastic strain	$\varepsilon^P = \int \ \dot{\boldsymbol{\varepsilon}}^P\ dt = \int \sqrt{\dot{\boldsymbol{\varepsilon}}^P : \dot{\boldsymbol{\varepsilon}}^P} dt = \int \dot{\lambda} dt$
ε_v^P	Plastic volumetric strain	$\varepsilon_v^P = \int \text{tr}\dot{\boldsymbol{\varepsilon}}^P dt = \int \dot{\lambda} \text{tr}\mathbf{M} dt$
η	Denominator in the tangent stiffness	$\eta = P_{ij}N_{ij} + H$
γ^P	Plastic distortional strain	$\gamma^P = \int \sqrt{\dot{\boldsymbol{\varepsilon}}^{Pd} : \dot{\boldsymbol{\varepsilon}}^{Pd}} dt = \int \dot{\lambda} \sqrt{\mathbf{M}^d : \mathbf{M}^d} dt$
$\dot{\lambda}$	Magnitude of the plastic strain rate (consistency parameter)	$\dot{\lambda} = \sqrt{\dot{\varepsilon}_{ij}^P \dot{\varepsilon}_{ij}^P}$
$\boldsymbol{\sigma}$	Stress tensor (conjugate to strain tensor $\boldsymbol{\varepsilon}$)	
τ	Characteristic response time in overstress rate dependence	

References

1. Anderson, Ch.E., Jr., Cox, P.A., Johnson, G.R., Maudlin, P.J.: *Comp. Mech.* **15**, 201 (1994)
2. Aubry, D., Hujeux, J.C., Lassoudier, F., Meimon, Y.: *Int. Symp. Numer. Meth. Geomech.* **3** (1982)
3. Bažant, Z.P.: *J. Eng. Mech. ASCE* **120**(3), 593 (1994)
4. Borja, R.I., Sama, K.M., Sanz, P.F.: *Comput. Meth. Appl. Mech. Eng.* **192**, 1227 (2003)
5. Brannon, R.M.: <http://www.me.unm.edu/~rnbrannon/gobag.html>
6. Brannon, R.M., Drugan, W.J.: *J. Mech. Phys. Solids* **41**, 297 (1993)
7. Brown, A.A., Casey, J., Nikkel, D.J., Jr.: *Int. J. Plasticity* **19**, 1965 (2003)
8. Brüning, M.: *Int. J. Plasticity* **18**, 1237 (2002)
9. Chadwick, P.: *Continuum Mechanics: Concise Theory and Problems*. Dover, Mineola, NY (1999)
10. Coulomb, C.A.: Essai sur une application des règles de maximis et minimis à quelques problèmes de statique relatifs à l'Architecture. In: *Memoires par Divers Savants*, pp. 1–40. Cambridge University Press, Cambridge (1972)
11. Dandekar, D.P.: A survey of compression studies on Silicon Carbide (SiC). Army Research Laboratory Technical Report ARL-TR-2695 (2002)
12. de Borst, R., Feenstra, P.H.: *Int. J. Numer. Meth. Eng.* **29**, 315 (1990)
13. de Borst, R., Heeres, O.M.: *Int. J. Numer. Anal. Meth. Geomech.* **26**, 1059 (2002)
14. Drucker, D.C.: *J. Colloid Sci.* **3**, 299 (1949)
15. Drucker, D.C.: *Q. Appl. Math.* **7**, 411 (1950)
16. Drucker, D.C.: In: *Proceedies of 1st Midwestern Conference on Solid Mechanics*. Urbana, p. 158 (1953)
17. Duva, J.M., Hutchinson, J.W.: Constitutive potentials for dilutely voided non-linear materials. *Mech. Mater.* **3**, 41 (1984)
18. Duvaut, G., Lions, J.L.: *Inequalities in Mechanics and Physics* (trans. C.W. John) Springer, Berlin Heidelberg New York (1976)
19. Ekh, M., Runesson, K.: *Int. J. Solids Struct.* **38**, 9461 (2001)
20. Etse, G., Willam, K.: *Eng. Comput.* **13**, 38 (1996)
21. Fleck, N.A., Kuhn, L.T., McMeeking, R.M.: *J. Mech. Phys. Solids* **40**, 1139 (1992)
22. Fossum, A.F., Brannon, R.M.: The Sandia GeoModel: Theory and User's Guide. Sandia National Laboratories Technical Report SAND2004-3226 (2004)
23. Fossum, A.F., Brannon, R.M.: On a viscoplastic model for rocks with mechanism-dependent characteristic times, *Acta Geotechnica* **1**(2), 89 (2006)
24. Gilman, J.J.: The plastic wave myth. In: Schmidt, S.C., Dick, R.D., Forbes, J.W., Tasker, D.G. (eds.) *Proceedings of SCCM-1991*, p. 387. Elsevier, New York (1992)
25. Gilman, J.J.: Mechanical states of solids. In: *Proceedings of SCCM-2001*, pp. 36–41. American Institute of Physics, New York (2002)
26. Grady, D.E., Young, E.G.: Evaluation of constitutive properties from velocity interferometry data. Sandia National Laboratories Report SAND75-0650 (1975)
27. Gurson, A.L.: *J. Eng. Mater. Technol. Trans. ASME* **99**, 2 (1977)
28. Hill, R.: *Q. J. Mech. Appl. Math.* **1**, 18 (1948)

29. Hill, R.: The Mathematical Theory of Plasticity. Wiley, New York (1950)
30. Hill, R.: Phil. Mag. **42**, 868 (1951)
31. Hill, R.: In: Hill, R., Sneddon, I.N. (eds.) Progress in Solid Mechanics, vol. **2**, p. 244. North-Holland, Amsterdam (1961)
32. Hill, R.: J. Mech. Phys. Solids **10**, 1 (1962)
33. Horie, Y.: J. Phys. IV France **110**, 3 (2003)
34. Iai, S.: Soils Found. **33**, 102 (1993)
35. Il'iushin, A.A.: Prikl. Math. Mekh. **25**, 503 (1961)
36. Johnson, G.R., Holmquist, T.J.: A computational constitutive model for brittle materials subjected to large strains, high strain rates and high pressures. In: Meyers, M.A., Murr, L.E., Staudhammer, K.P. (eds.) Shock Wave and High-Strain-Rate Phenomena in Materials, pp. 1075–1081. Dekker New York (1992)
37. Kabilamany, K., Ishihara, K.: Int. J. Soil Dyn. Earthq. Eng. **10**, 74 (1991)
38. Kailasam, M., Aravas, N., Ponte, P.: Castañeda, CMES **1**, 105 (2000)
39. Kleiber, M.: Comp. Meth. Appl. Mech. Eng. **90**, 943 (1991)
40. Koiter, W.T.: Q. Appl. Mech. **11**, 350 (1953)
41. Krieg, R.D., Key, S.W.: ASME AMD **20**, 125 (1976)
42. Krieg, R.D., Krieg, D.G.: J. Press. Vessel Technol. **99**, 510 (1977)
43. Lade, P.V., Bopp, P.A., Peters, J.F.: Mech. Mater. **16**, 249 (1993)
44. Lee, J.D., Chen, Y.: Theor. Appl. Fract. Mech. **35**, 187 (2001)
45. Lehmann, Th., Guo, Z.H., Liang, Y.H.: Eur. J. Mech. **48**, 35 (1991)
46. Levin, V.A., Lokhin, V.V., Zingerman, K.M.: J. Appl. Mech. **67**, 667 (2000)
47. Lubliner, J.: Plasticity Theory. MacMillian. New York, NY (1990)
48. Ma, F., Kishimoto, K.: Mech. Mater. **30**, 55 (1998)
49. Mähler, L., Ekh, M., Runesson, K.: Int. J. Plasticity. **17**, 943 (2001)
50. Mahnen, R.: Comput. Meth. Appl. Mech. Eng. **191**, 1611 (2002)
51. Maier, G., Hueckel, T.: Int. J. Rock Mech. Min. Sci. Geomech. Abstr. **16**, 77 (1979)
52. Malvern, L.E.: Introduction to the Mechanics of a Continua. Prentice-Hall, Englewood Cliffs, NJ (1969)
53. Mandel, J.: J. Mech. **1**, 3 (1962)
54. Mandel, J.: Conditions de stabilité et postulat de Drucker. In: Kravtchenko, J., Sirieys, P.M. (eds.) Rheology and Soil Mechanics. IUTAM Symposium, pp. 58–68. Springer, Berlin Heidelberg New York (1966)
55. Mandel, J.: Propagation des surfaces de discontinuité dans un milieu élasto-plastique. In: Kolsky, H., Prager, W. (eds.) Stress Waves in Anelastic Solids. IUTAM Symposium, pp. 331–341. Springer, Berlin Heidelberg New York (1964)
56. Mandel, J.: Int. J. Solids Struct. **1**, 273 (1965)
57. Marin, E.B., McDowell, D.L.: Int. J. Plasticity **12**(5), 629 (1996)
58. McLellan, A.G.: The Classical Thermodynamics of Deformable Materials. Cambridge University Press, London (1980)
59. Mehrabadi, M.M., Loret, B., Nemat-Nasser, S.: Proc. R. Soc. Lond. A **441**, 433 (1993)
60. Menzel, A., Ekh, M., Steinmann, P.: Int. J. Numer. Meth. Eng. **10**, 1409 (2002)
61. Mises, R.V.: Z. Angew. Math. Mech. **8**, 161 (1928)
62. Needleman, A. Rice, J.R.: Limits to ductility set by plastic flow localization. In: Koistinen, D.P., Wang, N.-M. (eds.) Mechanics of Sheet Metal Forming, pp. 237–267. Plenum, New York (1978)

63. Needleman, A., Rice, J.R.: *Mech. Mater.* **7**, 163 (1978)
64. Nemat-Nasser, S., Shokoh, A.: *Int. J. Solids Struct.* **16**, 495 (1980)
65. Ortiz, M., Popov, E.P.: *Int. J. Numer. Meth. Eng.* **21**, 1561 (1985)
66. Pan, J., Saje, M., Needleman, A.: *Int. J. Fract.* **2**, 261 (1983)
67. Pardoen, T., Hutchinson, J.W.: *J. Mech. Phys. Solids* **48**, 2467 (2000)
68. Perzyna, P.: Fundamental problems in viscoplasticity. In: *Advances in Applied Mechanics*, vol. **9**, pp. 243–377. Academic, New York (1966)
69. Preston, D.L., Tonks, D.L., Wallace D.C.: *J. Appl. Phys.* **93**, 211 (2003)
70. Prevost, J.H. Keane, C.M.: *J. Eng. Mech. ASCE* **116**, 1924 (1990)
71. Pučik, T.A.: A case study of instability and nonuniqueness induced by non-associated plastic flow. Unpublished Manuscript, Logicon RDA (1993)
72. Ragab, A.R., Saleh, A.R.: *Int. J. Plasticity.* **15**, 1041 (1999)
73. Rashid, M.: *Int. J. Numer. Meth. Eng.* **36**(23), 3937 (1993)
74. Reinhardt, W.D., Dubey, R.N.: *Mech. Res. Commun.* **22**, 165 (1995)
75. Rice, J.R.: The localization of plastic deformation. In: Koiter, W.T. (ed.) *Theoretical and Applied Mechanics*, pp. 207–220. North-Holland, Amsterdam (1976)
76. Rice, J.R., Tracy D.M.: Computational fracture mechanics. In: Fenves, S.J., et al. (eds.) *Symposiern on Numerical and Computer Methods in Structural Mechanics*, pp. 585–623. Academic, New York (1973)
77. Rudnicki, J.W., Rice, J.R.: *J. Mech. Phys. Solids* **23**, 371 (1975)
78. Sandler, I.S. Pučik, T.A.: *Mechanics of materials and structures. Stud. Appl. Mech.* **35**, 221 (1994)
79. Sandler, I.S., Rubin, D.: The consequences of non-associated plasticity in dynamic problems. In: Desai, C.S. (ed.) *Constitutive Laws for Engineering Materials – Theory and Applications*, p. 345. Elsevier, New York (1987)
80. Santaoja, K.: *Arch. Mech.* **55**, 501 (2003)
81. Schellekens, J.C.J., De Borst, R.: *Comp. Struct.* **37**, 1087 (1990)
82. Schajer, G.S.: *ASME J. Appl. Mech.* **65**, 1066 (1998)
83. Scheidler, M., Wright, T.W.: *Int. J. Plasticity.* **17**, 1033 (2001)
84. Schreyer, H.L., Kulak, R.F., Kramer, J.M.: *J. Press. Vessel Technol. ASME* **101**, 226 (1979)
85. Schreyer, H.L. Zuo, Q.H.: *J. Appl. Mech.* **62**, 780 (1995)
86. Sercombe, J., Ulm, F.J., Mang, H.A.: *Int. J. Numer. Meth. Eng.* **47**, 75 (2000)
87. Sevostianov, I., Kachanov, M.: *Int. J. Mater. Sci. Eng. A* **313**, 1 (2001)
88. Simo, J.C., Hughes, T.J.R.: *Computational Inelasticity*. Springer, Berlin Heidelberg New York (1998)
89. Simo, J.C., Kennedy, J.G., Govindjee, S.: *Int. J. Numer. Meth. Eng.* **26**, 2161 (1988)
90. Simo, J.C., Taylor, R.L.: *Comp. Meth. Appl. Mech. Eng.* **48**, 101 (1985)
91. Simo, J.C., Taylor, R.L.: *Int. J. Numer. Meth. Eng.* **22**, 649 (1986)
92. Stoughton, T.B.: *Int. J. Plasticity.* **18**, 687 (2002)
93. Swegle, J.W.: Grady, D.E.: *J. Appl. Phys.* **58**(2), 692 (1985)
94. Szabó, L.: *Int. J. Plasticity.* **13**, 809 (1998)
95. Taylor, G.I.: *Proc. R. Soc. Lond. A* **191**, 441 (1947)
96. Tsai, S.W., Hahn, H.T.: *Introduction to Composite Materials*. Technomic Publisher, Lancaster, PA (1980)
97. Tvergaard, V.: *J. Mech. Phys. Solids* **30**, 399 (1982)
98. Tvergaard, V.: *Int. J. Fract.* **18**, 237 (1982)
99. Tvergaard, V.: *J. Appl. Mech.* **66**, 3 (1999)

274 R.M. Brannon

100. Vermeer, P.A., de Borst, R.: *Heron* **29**, 3 (1984)
101. Wallace, D.C.: *Phys. Rev. B* **24**, 5597 (1981)
102. Wilkins, M.L.: Calculations of elastic–plastic flow. In: Alder, B. et al. (eds.) *Methods in Computational Physics*, vol. **8**, pp. 211–263. Academic, New York (1964)
103. Worswick, M.J., Pick, R.J.: *Mech. Mater.* **19**, 293 (1995)
104. Xiao, H., Bruhns, O.T., Meyers, A.: *Int. J. Plasticity* **16**, 143 (2000)
105. Yoder, P.J., Whirley, B.G.: *J. Appl. Mech. ASME* **51**, 283 (1984)
106. Zhao, Y.H., Tandon, G.P., Weng, G.J.: *Acta Mechanica* **76**, 105 (1989)
107. Zhenhaun, L., Minsheng, H., Cheng, W.: *Int. J. Solids Struct.* **40**, 3935 (2003)

ERRATA AND CLARIFICATIONS FOR...

Brannon, R. M. (2007). Elements of Phenomenological Plasticity: geometrical insight, computational algorithms, and applications in shock physics. **Shock Wave Science and Technology Reference Library: Solids I**, Springer-New York. 2: pp. 189-274.

- **CORRECTION TO MAIN TEXT:** The indicial formula in Eq. (6.35) is correct, but the “=” after **E** should be removed from the symbolic formula.
- **CORRECTION TO MAIN TEXT:** Two paragraphs above Fig. 6.3, the formulas for generating an octahedral profile were supposed to be typeset using *two* angles: an upper case Θ and a lower case θ (the Lode angle). The algorithm for generating an octahedral profile should read as follows:

Letting Θ denote the polar angle covering the entire range from 0° to 360° in the octahedral plane, compute $\theta = \frac{1}{3}\text{ArcSin}[\sin(3\Theta)]$. This lower case θ always falls between -30° to 30° because the principal ArcSin function always returns a result between -90° and $+90^\circ$. To generate the octahedral profile, parametrically plot

$$x = r(\theta)\cos\Theta \quad \text{and} \quad y = r(\theta)\sin\Theta.$$

Example: To make a plot of a Mohr-Coulomb profile, first note that the failure criterion may be written in terms of “cohesion” S_0 and “friction angle” ϕ parameters as

$$\frac{\sigma_H - \sigma_L}{2} = S_0 \cos\phi - \frac{\sigma_H + \sigma_L}{2} \sin\phi$$

Equations (6.18) and (6.20) may be substituted into this equation and solved for $r(z, \theta)$. Although complicated in its details, the final result may be written in the separable form

$$r(z, \theta) = \frac{R(z)}{\Gamma(\theta)}$$

Here,

$$R(z) = \frac{\sqrt{2}\cos\theta_0}{\cos(\theta_{\text{ref}} - \theta_0)} \left(S_0 \cos\phi - \frac{z}{\sqrt{3}} \sin\phi \right)$$

and

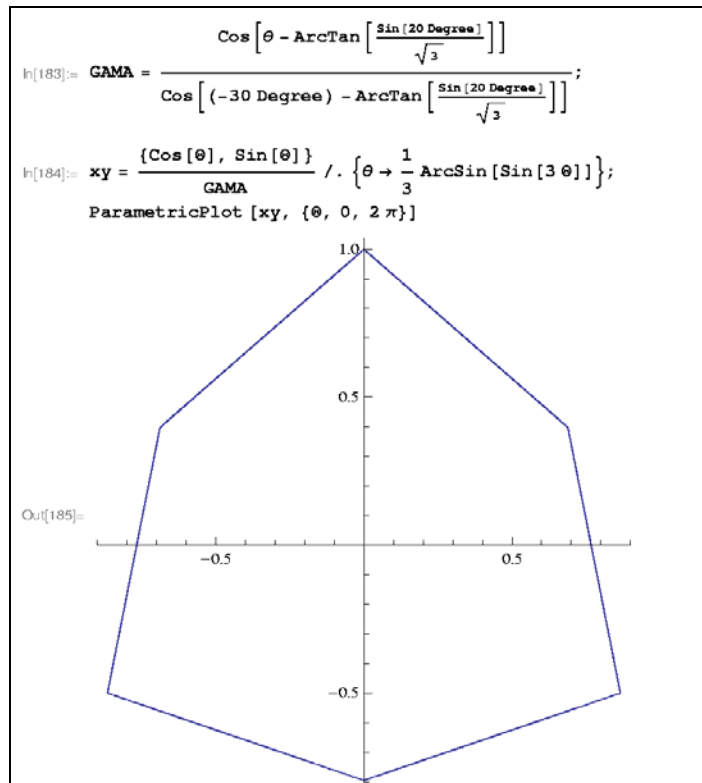
$$\Gamma(\theta) = \frac{\cos(\theta - \theta_0)}{\cos(\theta_{\text{ref}} - \theta_0)}, \quad \text{where } \theta_0 \equiv \text{ArcTan}\left(\frac{\sin\phi}{\sqrt{3}}\right).$$

The angle θ_{ref} is any selected value of the Lode angle at which it is desired for Γ to evaluate to unity. The angle θ_0 is the Lode angle at which the Lode radius is minimum (found by setting $\partial r/\partial\theta = 0$ and solving for θ). The function $R(z)$ quantifies the *size* of the octahedral profile, and $\Gamma(\theta)$ quantifies the *shape* of the profile.

The octahedral profile is generated by parametrically plotting

$$x = \frac{\cos \Theta}{\Gamma(\theta)} \quad \text{and} \quad y = \frac{\sin \Theta}{\Gamma(\theta)}, \quad \text{where} \quad \theta = \frac{1}{3} \text{ArcSin}[\sin(3\Theta)]$$

If, for example, $\phi = 20^\circ$ and $\theta_{\text{ref}} = -30^\circ$, then the octahedral profile may be generated in Mathematica as shown below.



- **CORRECTION TO MAIN TEXT:** The right-hand-side of Eq. (6.46) should be multiplied by $\hat{\lambda}$.
- **CORRECTION TO MAIN TEXT:** Throughout, there are several Greek letters typeset in bold that should be regular typeface (and vice versa).